Modeling gas-phase H2O between 5 μm and 540 μm toward massive protostars

Boonman, A.M.S.; Doty, S.D.; Dishoeck, E.F. van; Bergin, E.A.; Melnick, G.J.; Wright, C.M.; Stark, R.

A&A 406, 937–955 (2003)
DOI: 10.1051/0004-6361:20030765

Astronomy & Astrophysics

Modeling gas-phase H_2O between 5 μm and 540 μm toward massive protostars⋆

A. M. S. Boonman[1], S. D. Doty[2], E. F. van Dishoeck[1], E. A. Bergin[3], G. J. Melnick[3], C. M. Wright[1,⋆⋆], and R. Stark[4]

[1] Sterrewacht Leiden, PO Box 9513, 2300 RA Leiden, The Netherlands
[2] Department of Physics and Astronomy, Denison University, Granville, Ohio 43023, USA
[3] Harvard-Smithsonian Center for Astrophysics, 60 Garden Street, Cambridge, MA 02138, USA
[4] Max-Planck-Institut für Radioastronomie, Auf dem Hügel 69, 53121 Bonn, Germany

Received 10 March 2003 / Accepted 16 May 2003

Abstract. We present models and observations of gas-phase H_2O lines between 5 and 540 μm toward deeply embedded massive protostars, involving both pure rotational and ro-vibrational transitions. The data have been obtained for 6 sources with both the Short and Long Wavelength Spectrometers (SWS and LWS) on board the Infrared Space Observatory (ISO) and with the Submillimeter Wave Astronomy Satellite (SWAS). For comparison, CO $J = 7-6$ spectra have been observed with the MPIfR/SRON 800 GHz heterodyne spectrometer at the James Clerk Maxwell Telescope (JCMT). A radiative transfer model in combination with different physical/chemical scenarios has been used to model these H_2O lines for 4 sources to probe the chemical structure of these massive protostars. The results indicate that pure gas-phase production of H_2O cannot explain the observed spectra. Ice evaporation in the warm inner envelope and freeze-out in the cold outer part are important for most of our sources and occur at $T \sim 90$–110 K. The ISO-SWS data are particularly sensitive to ice evaporation in the inner part whereas the ISO-LWS data are good diagnostics of freeze-out in the outer region. The modeling suggests that the 557 GHz SWAS line includes contributions from both the cold and the warm H_2O gas. The SWAS line profiles indicate that for some of the sources a fraction of up to 50% of the total flux may originate in the outflow. Shocks do not seem to contribute significantly to the observed emission in other H_2O lines, however, in contrast with the case for Orion. The results show that three of the observed and modeled H_2O lines, the $3_{03}-2_{12}$, $2_{12}-1_{01}$, and $1_{10}-1_{01}$ lines, are good candidates to observe with the Herschel Space Observatory in order to further investigate the physical and chemical conditions in massive star-forming regions.

Key words. ISM: abundances – ISM: molecules – infrared: ISM – ISM: lines and bands – molecular processes

1. Introduction

Space missions such as the Infrared Space Observatory (ISO) and the Submillimeter Wave Astronomy Satellite (SWAS) have provided a wealth of data on chemically important molecules like H_2O that are difficult to observe from the ground. Water is a particularly interesting molecule to study the interaction of a protostar with its environment, since its abundance reacts strongly to the temperature changes associated with star formation (e.g., Hollenbach & McKee 1979; Charnley 1997). In the coldest regions, the molecule is known to be present in ice mantles on grains, whereas it evaporates back into the gas phase when the dust temperature rises above ~100 K. In even warmer regions and shocks, all gas-phase oxygen not locked up in CO is driven into H_2O, predicting greatly enhanced gas-phase H_2O abundances (e.g., Kaufman & Neufeld 1996; Charnley 1997). The excitation of H_2O also differs from that of other molecules, in particular from that of heavy rotors, since both collisions and infrared radiation from warm dust influence the level populations.

We use here observations of H_2O combined with detailed radiative transfer modeling to constrain its excitation and chemical structure in the envelopes of a sample of massive protostars. The data set is unique, because three different observational techniques are used: mid-infrared ro-vibrational absorption at 6 μm with the Short Wavelength Spectrometer (SWS) on ISO; far-infrared pure rotational emission or absorption with the Long Wavelength Spectrometer (LWS) on ISO; and submillimeter pure rotational emission with SWAS. Each of these wavelength regions probes a different part of the envelope. Such combined data are not available for low-mass protostars.

Since the launches of ISO and SWAS, there have been several publications of H_2O observations toward massive protostars using each of these wavelength regions individually.

Send offprint requests to: A. M. S. Boonman,
e-mail: boonman@strw.leidenuniv.nl

⋆ Based on observations with ISO, an ESA project with instruments funded by ESA Member States (especially the PI countries: France, Germany, The Netherlands and UK) and with the participation of ISAS and NASA.

⋆⋆ Visiting scientist.

For example, Helmich et al. (1996), van Dishoeck & Helmich (1996), and Boonman & van Dishoeck (2003) found strong H_2O absorption in the ν_2 ro-vibrational band toward a dozen objects, indicating gas-phase H_2O abundances of $\sim 10^{-5}$ in the warm gas along the line of sight. In contrast, SWAS observations of the lowest $1_{10}-1_{01}$ 557 GHz line in emission toward some of the same sources indicate rather low H_2O abundances of $\sim 10^{-9}$ to a few $\times 10^{-8}$, but in a much larger beam (Snell et al. 2000; Ashby et al. 2000). Except for Orion-KL and SgrB2 (see below), few H_2O lines in ISO-LWS spectra of massive protostars have yet been reported (Wright et al. 1997), in contrast with the case for low-mass protostars (see Nisini et al. 2002 for a summary). One of the purposes of this paper is to add the ISO-LWS information to the above studies.

The best studied massive star-forming object is Orion-KL, where a wealth of H_2O lines has been detected using all three instruments. ISO-SWS spectra show both absorption and emission in the ro-vibrational 6 μm band (van Dishoeck et al. 1998; González-Alfonso et al. 1998), as well as a series pure rotational absorption lines at 25–45 μm (Wright et al. 2000). Above 45 μm, the pure rotational lines are seen in emission in the larger ISO-LWS beam (Harwit et al. 1998; Cernicharo et al. 1999). The line profiles are resolved with the Fabry-Pérot and indicate the presence of H_2O with abundances of $\sim 10^{-4}$ in the outflowing gas. Melnick et al. (2000b) find similar H_2O abundances in the shocked gas surrounding IRc2 with SWAS, but much lower abundances of a few 10^{-8} in the extended ridge. The velocity resolution of SWAS is much higher (<1 km s^{-1}) than that of ISO, thus allowing the shocked and quiescent gas to be distinguished.

The other well-studied massive star-forming region is SgrB2. Although it is located at a much greater distance than Orion and the sources studied in this work, strong H_2O lines have been detected. Most are seen in absorption (e.g., Cernicharo et al. 1997), and arise in the dense warm shell and colder foreground clouds along the line of sight toward SgrB2 at an abundance of $\sim 10^{-5}$. One of the questions addressed in this paper is whether the H_2O observations of Orion and SgrB2 are characteristic of other massive protostars.

Theoretical models based on both shock chemistry and quiescent chemistry have been developed in order to explain these large differences in observed H_2O abundances. Non-dissociative shock models readily predict H_2O abundances of order 10^{-4} in the hot ~2000 K gas produced by gas-phase reactions of $O + H_2 \rightarrow OH + H$ and $OH + H_2 \rightarrow H_2O + H$, consistent with the Orion observations (e.g., Draine et al. 1983; Kaufman & Neufeld 1996). Such high abundances can be maintained in the post-shock gas up to $t \sim 10^5$ yr (Bergin et al. 1998). On the other hand, quiescent gas-phase chemical models also predict H_2O abundances of up to $\sim 10^{-4}$ for $T \gtrsim 230$ K by the same reactions (Charnley 1997; Doty et al. 2002). Therefore both quiescent high-temperature chemistry and shock chemistry can in principle explain the high H_2O abundances observed.

Quiescent low-temperature (<230 K) gas-phase chemistry gives typical H_2O abundances of a few $\times 10^{-7}$ (e.g., Lee et al. 1996; Le Teuff et al. 2000). Here the H_2O is formed by ion-molecule reactions starting with $O + H_3^+$ or $O^+ + H_2$ producing OH^+. A series of rapid H-abstraction reactions with H_2 then leads to H_3O^+ which dissociatively recombines to H_2O. The H_2O abundances produced by this scheme are a factor of at least ~10 higher than the observed abundances toward high-mass star-forming regions by Snell et al. (2000). This has led Bergin et al. (2000) to propose that significant freeze-out of many species, including H_2O and its precursors, must occur in the cold gas. Doty et al. (2002) have coupled the gas-phase chemistry with a physical model of a massive protostellar envelope and show that besides freeze-out also beam dilution and the non-constancy of the H_2O abundance throughout the envelope may play a role. Water ice has been observed toward many star-forming regions (e.g., Smith et al. 1989; Keane et al. 2001) and comparison of gas-phase and solid-state H_2O abundances shows that sources with the high gas-phase H_2O abundances have relatively low H_2O ice abundances, providing observational evidence for grain-mantle evaporation (van Dishoeck & Helmich 1996; Boonman & van Dishoeck 2003). Fraser et al. (2001) find that H_2O ice evaporates around ~90–110 K for $t \lesssim 10^3$ yr, temperatures that are easily reached in the envelopes of massive protostars (van der Tak et al. 2000b).

An alternative model for the low abundances of H_2O in massive star-forming regions has been put forward by Spaans & van Dishoeck (2001), who suggest that enhanced photodissociation in an inhomogeneous "clumpy" cloud may be responsible. Such models may apply to large-scale molecular clouds, but are not applicable to the immediate surroundings of the deeply-embedded massive protostars studied here.

In this paper we combine the H_2O spectra between 5 and 200 μm from the ISO-SWS and LWS with the SWAS data for a sample of 6 massive protostars in order to find a chemical scenario that can explain all H_2O observations for these sources between ~5 and 540 μm. Some of these data have been presented previously by Snell et al. (2000), Boonman et al. (2000), and Boonman & van Dishoeck (2003). A state-of-the-art model including the detailed physical structure of the circumstellar envelopes is used, combined with an extensive chemical network. Both pure gas-phase chemistry and gas-grain interactions, such as ice evaporation and freeze-out onto the grains, are investigated.

The paper is organized as follows: Sect. 2 describes the observations and the reduction of the different data sets as well as a short description of the source sample. In Sect. 3 the profiles of the H_2O $1_{10}-1_{01}$ SWAS lines are compared with those of the CO $J = 7$–6 lines toward the same sources. The radiative transfer model, and the adopted physical and chemical models are described in Sect. 4. The detailed results for AFGL 2591 are presented in Sect. 5 and those for the other sources in Sect. 6. Section 7 discusses the differences and similarities found between the sources, the comparison with shock models, and some future prospects for the Herschel Space Observatory. Finally, the conclusions are presented in Sect. 8.

2. Observations and reduction

2.1. Source sample

The sources in our sample are all deeply embedded massive protostars chosen to be bright at mid-infrared wavelengths and

Table 1. Overview of ISO-LWS and SWAS observations.

Source	ISO-LWS observations		SWAS observations	
	observation number	observing mode	observing period	integration time
AFGL 2591	52 800 108	LWS04	1999, Jun. 25 – Dec. 17[a]	54.7 hr
NGC 7538 IRS9	57 100 914	LWS04	2000, Jul. 16 – Aug. 10	50.5 hr
W 3 IRS5	47 301 306	LWS04	2000, Aug. 11 – 13	10.7 hr
S 140 IRS1	36 802 110	LWS04	1998, Dec. 20 – 1999, Jul. 21[a]	18.3 hr
NGC 7538 IRS1	84 201 112	LWS04	2001, Jul. 13 – 19	18.8 hr
MonR2 IRS3	–	–	2001, Sep. 19 – Oct. 8	17.6 hr

[a] Snell et al. (2000).

relatively nearby. They have weak radio continuum emission and are not yet in the ultracompact H II region phase. Outflows are known to be associated with all sources. Their luminosities range from $\sim 10^4$–$2 \times 10^5\ L_\odot$ and their distances from 0.8–2.8 kpc (van der Tak et al. 2000b, and references therein). Five of the sources are a sub-set of a larger sample of massive protostars studied both at submillimeter and infrared wavelengths and in gas-phase species as well as ices (e.g. Gerakines et al. 1999; van der Tak et al. 2000b; Lahuis & van Dishoeck 2000; Boogert et al. 2000; Boonman et al. 2003). To this sample, we have added MonR2 IRS3, which shows similar characteristics (e.g. Giannakopoulou et al. 1997; Keane et al. 2001). Van der Tak et al. (2000b, 2003) have constrained the temperature and density gradients in the molecular envelopes of these sources from submillimeter line and continuum data (see Sect. 4.1).

2.2. ISO-SWS and -LWS

The H_2O ν_2 ro-vibrational spectra around $\sim 6\ \mu$m observed with ISO-SWS have been discussed in a previous paper by Boonman & van Dishoeck (2003). Because the ISO-SWS absorption data sample a pencil-beam line of sight toward the source, they are weighted toward the warmer gas in the inner envelope. Strong H_2O absorption with excitation temperatures of $\gtrsim$250 K has been detected toward AFGL 2591 and MonR2 IRS3, whereas no H_2O absorption is seen toward NGC 7538 IRS9. The inferred H_2O abundance in the warm gas ranges from $\sim 5 \times 10^{-6}$ to $\sim 6 \times 10^{-5}$, and has been found to correlate with the temperature of the warm gas and the H_2O gas/solid ratio (Boonman & van Dishoeck 2003).

The observation log of the pure rotational H_2O lines from ISO-LWS is summarized in Table 1. The ISO-LWS beam size varies between $\sim 66''$ and $\sim 78''$ in diameter and is therefore more sensitive to the cold outer envelope. Data reduction was done within the ISO Spectroscopic Analysis Package (ISAP version 2.0) and the LWS Interactive Analysis (LIA version 8.0) package using the ISO Off-line Processing (OLP version 10) software. The spectra were taken in the high-resolution Fabry-Pérot LWS04 observing mode toward 5 of the sources. For MonR2 IRS3, no LWS04 observations have been performed. The LWS04 data have been reduced using the standard pipeline reduction, followed by a correction for inaccurate grating positioning. The dark current values have not been adjusted to those of the LWS01 low-resolution grating scan of the same source, since only for half of the sources this grating scan is taken in the same revolution as the LWS04 Fabry-Pérot observations. Comparing the continuum levels of the LWS04 and LWS01 observations shows that the LWS04 continuum is within ~30% of the LWS01 continuum for all H_2O lines in AFGL 2591 and S 140 IRS1, and for most lines in NGC 7538 IRS9, NGC 7538 IRS1, and W 3 IRS5, which is in agreement with the quoted calibration uncertainty of the LWS01 fluxes of ~30% (Swinyard et al. 1996). For NGC 7538 IRS9 and W 3 IRS5, the LWS04 continuum near H_2O lines with $\lambda \gtrsim 136\ \mu$m is about twice as high as that found from the LWS01 spectra. For NGC 7538 IRS1 the LWS04 continuum of H_2O lines between 132 and 139 μm is ~50% higher than the LWS01 continuum. Therefore the accuracy of the LWS04 continuum levels is estimated to be ~50% for the latter lines.

The spectra have been flat-fielded and rebinned, using the ISO-SWS Interactive Analysis System, to a spectral resolution of $\lambda/\Delta\lambda = 18\,000$, about twice the nominal spectral resolution. The resulting spectra have been used to determine the 3σ noise levels and the line fluxes for the (tentative) detections.

Adjusting the continuum levels of the LWS04 observations to those of the LWS01 observations does not change the line fluxes of the (tentative) detections nor the derived 3σ upper limits by more than 5%. This is negligible compared to the 1σ noise of the spectra and the calibration uncertainty of the line fluxes which is ~30%.

A selection of the final LWS spectra is shown in Fig. 1. The spectra of the H_2O lines not shown are qualitatively similar. The only firm detection is the H_2O 3_{03}–2_{12} line at 174.6 μm in emission toward S 140 IRS1. Two tentative detections are the H_2O 2_{21}–1_{10} line at 108.1 μm in absorption toward AFGL 2591 and W 3 IRS5, and the H_2O 4_{23}–4_{14} line at 132.4 μm in emission toward NGC 7538 IRS1. The spectrum of the H_2O 2_{12}–1_{01} line at 179.5 μm toward NGC 7538 IRS9 seems to show a 3σ absorption. However, this spectrum has the weakest continuum of all sources, which is still about twice as high as the corresponding LWS01 continuum level for this source (see above), and the absorption falls to negative values. Therefore, we do not trust this absorption and use the 3σ upper limit for comparison with predicted line fluxes instead.

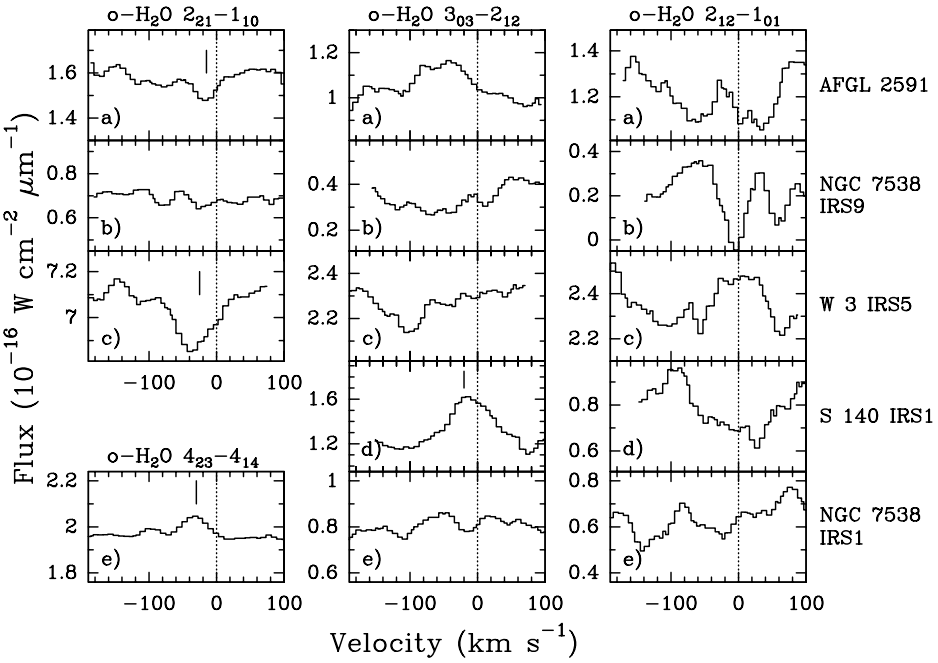

Fig. 1. Overview of the ISO-LWS data for a selection of the ortho-H_2O $2_{21}-1_{10}$, $4_{23}-4_{14}$, $3_{03}-2_{12}$, and $2_{12}-1_{01}$ lines at 108.1 μm, 132.4 μm, 174.6 μm, and 179.5 μm respectively, in **a)** AFGL 2591, **b)** NGC 7538 IRS9, **c)** W 3 IRS5, **d)** S 140 IRS1, and **e)** NGC 7538 IRS1. The vertical markers indicate the (tentative) detections. All lines have been corrected for the $V_{\rm LSR}$ of the source and the resolution of the spectra is $\Delta V \sim$ 30 km s^{-1}. The vertical dotted lines indicate the positions of the H_2O lines if they are at the $V_{\rm LSR}$ of the source. The deviations of the (tentative) detections from the dotted lines are about the spectral resolution. The ortho-H_2O $2_{21}-1_{10}$ line has not been observed toward S 140 IRS1. Note that the flux scale in the panel of the $3_{03}-2_{12}$ line in S 140 IRS1 covers twice as large a range as in all other panels.

The ISO LWS01 low resolution ($\lambda/\Delta\lambda \approx 200$) full 45–197 μm grating scans of the sources have been inspected as well, but they show primarily [C II] and [O I] fine-structure lines. No H_2O lines are seen down to $\sim 10^{-18}$ W cm^{-2} and high-J CO lines are only detected toward W 3 IRS5 (Wright et al. 1997). This is in strong contrast with low-mass YSOs, where H_2O and/or OH lines are readily detected in the low-resolution grating scans (e.g., Nisini et al. 1999; Spinoglio et al. 2000).

2.3. SWAS

The observations of the H_2O $1_{10}-1_{01}$ line at 556.936 GHz with SWAS have been carried out between December 1998 and October 2001. The integration times varied between ~17 hr and ~55 hr (Table 1).

The data have been reduced using the SWAS pipeline (Melnick et al. 2000a). The resulting scans have then been averaged for each source within the Continuum and Line Analysis Single-dish Software (CLASS) package. Subsequently, a first order baseline has been subtracted and the spectra have been corrected for the main beam efficiency of 0.90 and set to the correct velocity of the source. Typical rms noise levels are ~10–30 mK. The resulting spectra have a velocity resolution of ~1 km s^{-1} and a channel spacing of 0.6 km s^{-1}. The SWAS beam is elliptical with angular dimensions of $3'.3 \times 4'.5$ at the frequency of the H_2O line. The calibration uncertainty is ~5% (Melnick et al. 2000a) and the total uncertainty in the integrated intensity is estimated to be ~10%, based on the comparison of [C I] ground-based versus space observations (Melnick et al. 2000a). The SWAS spectra are presented in Fig. 2. The data on AFGL 2591 and S 140 IRS1 have been presented previously by Snell et al. (2000) and are included here.

2.4. CO J = 7–6

In addition to the H_2O spectra, CO J = 7–6 lines have been obtained for the same sources to constrain the warm outflowing gas. The lines have been observed with the MPIfR/SRON 800 GHz heterodyne spectrometer at the James Clerk Maxwell Telescope (JCMT)[1] in April 2000. The beam size of this instrument is ~8″ full width at half maximum (FWHM) and the main beam efficiency is 0.2. The absolute calibration uncertainty is estimated at 50%. Details on this instrument can be found in Stark et al. (in preparation). The spectra have been analyzed in a similar way as the SWAS observations. The resulting spectra have been smoothed to a resolution of ~0.9 km s^{-1}, whereas the instrumental resolution is ~0.14 km s^{-1}. Typical rms noise levels in the final spectra are less than 1 K on the $T_{\rm A}^*$ scale after 20 min of integration. The spectrum toward AFGL 2591 has a lower noise level, since the integration time is twice as long as for the other sources. The CO spectra are presented in Fig. 2. The AFGL 2591 spectrum has been shown previously by Boonman et al. (2001).

[1] The James Clerk Maxwell Telescope is operated by the Joint Astronomy Centre, on behalf of the Particle Physics and Astronomy Research Council of UK, The Netherlands Organization for Scientific Research, and the National Research Council of Canada.

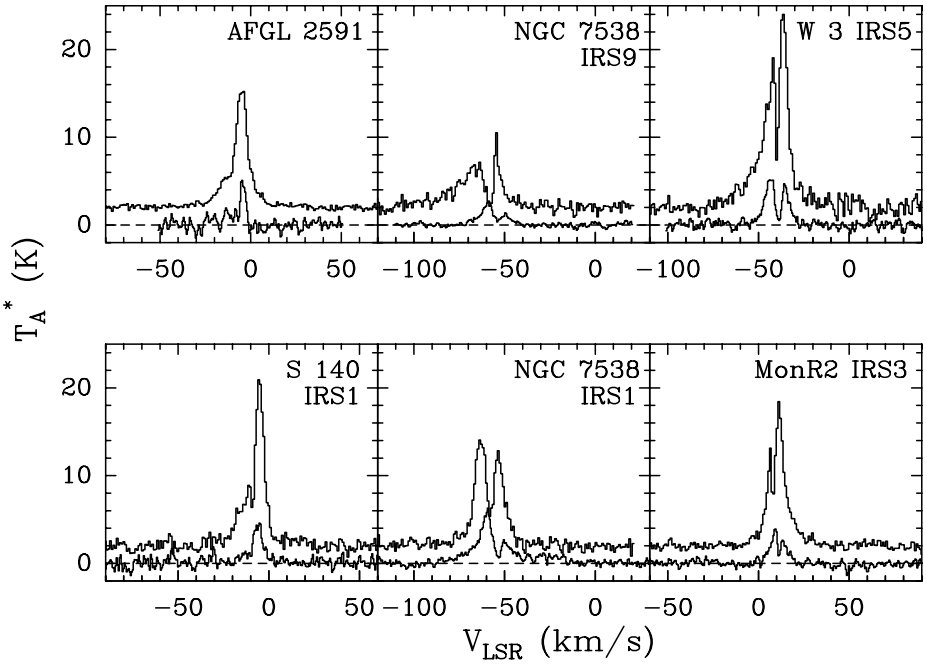

Fig. 2. Continuum subtracted spectra of the CO J = 7–6 lines (JCMT) compared with the H_2O 1_{10}–1_{01} lines (SWAS). The CO lines have been shifted upwards by 2 K for clarity. The H_2O lines have been multiplied by a factor of 20, except that for AFGL 2591 which is multiplied by 80. Both spectra have been binned to a spectral resolution of ∼0.9 km s^{-1} (see text).

3. CO J = 7–6 versus H_2O 1_{10}–1_{01} line profiles

The CO J = 7–6 and H_2O 1_{10}–1_{01} lines have been detected toward all sources in our sample and show similar profiles, even though they refer to orders of magnitude different beams (Fig. 2). The ratio of the peak intensities is also similar for all sources. The integrated intensities have been calculated for both lines and are listed in Table 2. Those sources that show self-absorbed CO J = 7–6 lines also have self-absorbed H_2O 1_{10}–1_{01} lines. The line profiles toward AFGL 2591 and S 140 IRS1 show only one clear narrow peak. For H_2O, this narrow peak appears to be shifted with respect to the V_{LSR} of the envelope by ∼1 km s^{-1}. The CO J = 7–6 line toward S 140 IRS1 shows some evidence for an additional blue-shifted peak. This may indicate that the intrinsic H_2O lines are broader for AFGL 2591 and S 140 IRS1 but that the blue peak is almost completely absorbed by foreground gas. Mitchell et al. (1992) show that there is a foreground cloud at 0 km s^{-1} for AFGL 2591 and van der Tak et al. (1999) see additional absorption at −8.0 km s^{-1} for the low-J CO lines, which they attribute to cold gas intrinsic to the source. Thus, the integrated intensities for AFGL 2591 and S 140 IRS1 may be lower limits, and the actual value for the 557 GHz line toward AFGL 2591 may be up to a factor of ∼2 higher.

The CO J = 7–6 lines have a clear wing component due to the outflow toward all sources. It is also present in the H_2O 1_{10}–1_{01} lines toward W 3 IRS5, MonR2 IRS3, NGC 7538 IRS1, and NGC 7538 IRS9. The CO J = 7–6 lines arise from an energy level at 155 K above the ground state, whereas the H_2O 1_{10}–1_{01} lines arise from a level at 61 K. The similarities of the H_2O 1_{10}–1_{01} and CO J = 7–6 line profiles may indicate that both lines trace gas warmer than $T \sim 61$ K. For the two sources in NGC 7538, a shift in the SWAS spectra of ∼4 km s^{-1} to the red is observed compared with the CO J = 7–6 data. A similar shift has been observed for the CO J = 3–2 lines in these sources by Mitchell & Hasegawa (1991). They attribute the red peak of the CO J = 3–2 emission to a foreground cloud at −49 km s^{-1}, which also corresponds to the velocity of the red H_2O 1_{10}–1_{01} peak. However, the red peak of the CO J = 3–2 line is much narrower than the corresponding blue peak, whereas they are comparable for the 557 GHz line. It is unclear whether the red H_2O 1_{10}–1_{01} peak is associated with the foreground cloud or with IRS9 and IRS1; here the latter is assumed in the analysis, and therefore the integrated flux of the 557 GHz line toward these sources may be overestimated. The line wings and the narrow peaks are fit with gaussians and the corresponding parameters are listed in Table 2. In general the widths of the H_2O 1_{10}–1_{01} wing seem to be somewhat smaller than that for the CO J = 7–6 line.

For W 3 IRS5, the H_2O wing component contains at most ∼15% of the total integrated intensity, close to the calibration uncertainty. Therefore, using the total integrated intensity, instead of the narrow component only, for comparison with the predictions from chemical scenarios does not affect our conclusions for this source. For the other three sources that show a H_2O 1_{10}–1_{01} line wing, its integrated intensity could contain about half of the total flux. However, these sources likely show contamination by other nearby objects and/or a foreground cloud (see above), and thus less weight has been assigned to the 557 GHz line in the determination of the preferred chemical scenario. Therefore, the choice of the best chemical scenario is not affected by the inclusion of a possible wing component in the 557 GHz line.

The observed widths of the 557 GHz narrow components (Table 2) are not much broader than the turbulent line widths

Table 2. Gaussian fit parameters for the CO J = 7–6 and H_2O 1_{10}–1_{01} lines.

Source	CO J = 7–6			H_2O 1_{10}–1_{01}			
	$\int T_{MB}\Delta V^a$	ΔV_{wing}	V^b_{LSR}	$\int T_{MB}\Delta V^a$	ΔV^c_{wing}	ΔV^d_{peak}	V^b_{LSR}
	K km s^{-1}	km s^{-1}	km s^{-1}	K km s^{-1}	km s^{-1}	km s^{-1}	km s^{-1}
AFGL 2591[e]	972	21	–4.8[f]	0.37[g]	–	3.4	–4.6[e]
NGC 7538 IRS9	796	40	–57.7	1.62	~22	7	–54.0
W 3 IRS5	2000	31	–39.7	3.27	~20	5.0	–38.6
S140 IRS1[e]	1100	38	–8.6	1.94	–	5.3	–6.0[e]
NGC 7538 IRS1	1200	28	–57.9	5.32	~33	7	–53.6
Mon R2 IRS3	1070	17	8.3	1.91	~13	3.5	11.4

[a] Integrated intensity of whole feature, unless otherwise noted.
[b] Position of the self-absorption, unless otherwise noted.
[c] Estimate; uncertain fit.
[d] FWHM of the narrow peak. In case of a self-absorbed line profile the average of the two peak components is listed.
[e] Using the H_2O 1_{10}–1_{01} data from Snell et al. (2000).
[f] Parameters of the narrow peak only.
[g] Integrated intensity between −16.2 and −0.8 km s^{-1}.

used in the models (see Sect. 4.1). If a steep velocity gradient would be present, such as expected in a molecular outflow or strong infall, the narrow peaks of the self-absorbed lines are expected to be much broader than the turbulent width. High optical depths can however also play a role. The different chemical scenarios discussed in the following sections predict optical depths at line center of τ >1000, which, combined with the low intensities, indicates that the 557 GHz emission is thermalized and does not fill the SWAS beam.

4. H_2O modeling

4.1. Model description

The models considered here adopt a quiescent H_2O chemistry within a protostellar envelope and do not include shocks. Such models are appropriate for AFGL 2591 and S 140 IRS1, for which the SWAS H_2O line profiles do not show evidence for outflows. For the other sources, they can be used to investigate to what extent both high- and low-T quiescent chemistry can reproduce the observations. The fraction of H_2O originating from shocks is likely to be modest based on the SWAS line profiles (see Sect. 3).

The adopted physical models use the dust properties, density profiles, outer radii, and source parameters identified by van der Tak et al. (2000b, 2003). The radiative transfer through the dust is solved self-consistently to compute the dust temperature. The gas temperature profile is calculated using methods described by Doty & Neufeld (1997) and Doty et al. (2002). As noted in these studies, the gas and dust temperatures are well-coupled, with the gas temperature almost always within 20 K of the dust temperature (and generally much closer). Assuming that the gas temperature equals the dust temperature does not change our results significantly. The calculations use collisional rate coefficients from Phillips & Green (1995) and Green et al. (1993).

The chemistry is calculated at each of the 237 radial points in the envelope until the gas-phase chemistry has reached equilibrium, using the gas temperature and density at that point. It is assumed that the maximum H_2O abundance available in gas or ice is $n(H_2O)/n(H_2) = 2 \times 10^{-4}$. In the case of ice evaporation, this process is taken to occur instantaneously. The adopted chemical model has been described by Doty & Neufeld (1997) and Doty et al. (2002).

Given the H_2O abundances and the kinetic temperature profile, the radiative transfer including both the dust and gas is solved self-consistently using an approximate lambda iteration (ALI) model described in Doty & Neufeld (1997). This code has been tested against other radiative transfer codes and the results are found to agree to within 2% for optically thin lines, with somewhat higher deviations possible for highly optically thick lines (van Zadelhoff et al. 2002). The radiative transfer model includes the lowest 25 energy levels of p-H_2O and o-H_2O up to energies of ~1100 K. No systematic velocity gradient is included but a turbulent linewidth corresponding to a Doppler parameter b of 2 km s^{-1} is assumed, comparable to the observed $C^{17}O$ and CS submillimeter line widths. For more detailed information see Doty & Neufeld (1997) and van Zadelhoff et al. (2002) and references therein.

The pure rotational line fluxes are computed with the ALI code and convolved with the appropiate telescope beam to produce simulated observations, using the spectral resolution of the data given in Sects. 2.2 and 2.3. These results can then be compared directly to the ISO-LWS and SWAS observations. For the ISO-LWS data, the line fluxes are presented in W cm^{-2} μm^{-1}. To convert to W cm^{-2}, the tabulated fluxes should be multiplied by $\Delta\lambda = \lambda/R$ in μm, with $R \approx 9200$.

For the ISO-SWS comparison, synthetic spectra for the ν_2 = 1–0 ro-vibrational absorption band of H_2O around 6 μm can be calculated from the resulting level populations. The spectral resolution is $\lambda/\Delta\lambda \approx 1400$, with $\Delta\lambda \sim 0.0042\,\mu$m. The density in each level is integrated along the line of sight through the molecular envelope using a linewidth corresponding to a

Table 3. Summary of chemical scenarios investigated in this work.

Scenario	Ice evaporation	Freeze-out	Cold gas-phase H_2O
1	NO	NO	YES, via chemistry
2	YES, T = 100 K	NO	YES, via chemistry
3	YES, T = 110 K	YES, T < 110 K	NO, $x(H_2O) \sim 0$
4	YES, T = 90 K	YES, T < 90 K	NO, $x(H_2O) \sim 0$
5	YES, T = 100 K	YES, T < 100 K	NO, $x(H_2O) \sim 0$
6	NO	YES, T < 100 K	NO, $x(H_2O) \sim 0$
7	YES, T = 100 K	YES, T < 100 K	YES, $x(H_2O) \sim 10^{-10}$
8	YES, T = 100 K	YES, T < 100 K	YES, $x(H_2O) \sim 10^{-8}$
9	YES, T = 100 K	YES, T < 100 K	YES, $x(H_2O) \sim 10^{-7}$

Doppler parameter b between 1.5 and 5 km s^{-1}. The effect of emission possibly filling in the absorption is not included here, but has been discussed in Boonman & van Dishoeck (2003). They show that the H_2O column densities in the warm gas needed to fit the data increase by at most factors of ~3–6 when emission is included.

4.2. Chemical scenarios

Different chemical processes may influence the abundance of gas-phase H_2O. These include pure gas-phase chemistry, ice evaporation, freeze-out of H_2O and its precursors onto the grains, and the possible existence of cold gas-phase H_2O at temperatures below the nominal freeze-out temperature. Water ice has been detected toward all sources in our sample at an abundance of $\sim(0.2–2) \times 10^{-4}$ with respect to molecular hydrogen, indicating that freeze-out and grain-surface chemistry is important (Keane et al. 2001; Smith et al. 1989; Gibb & Whittet 2002). The H_2O ice itself is thought to form mostly through grain surface reactions of oxygen and hydrogen, rather than direct freeze-out of gas-phase H_2O. In our models, the term "freeze-out" simply reflects a low gas-phase H_2O abundance due to a combination of these processes.

Van der Tak et al. (2000b) found that gas at temperatures higher than the H_2O evaporation limit of ~90–110 K is present in all sources. Therefore it is expected that at least for the ν_2 ro-vibrational band of H_2O, ice evaporation plays a role, since this band probes mainly the warmer gas at $T \gtrsim 100$ K (see Boonman & van Dishoeck 2003). Models with and without evaporation of H_2O ice are investigated to test the sensitivity of the various data sets to this process.

Similarly, models with and without freeze-out are considered. The effects of freeze-out are expected to be largest for the pure rotational H_2O lines which sample the more extended cold envelope. Since the SWAS observations suggest that a low level of cold H_2O gas may be present (Snell et al. 2000), we also consider the possibility that H_2O is only partially frozen-out onto the grains, or that some non-thermal desorption mechanism maintains a low gas-phase H_2O abundance.

Models with different combinations of the chemical processes described above have been developed. These chemical scenarios are summarized in Table 3. In the case of total freeze-out, the H_2O abundances below the evaporation temperature T_{evap} are set to very low values of $\sim 10^{-12}$. If only partial freeze-out is assumed, H_2O abundances in between those of total freeze-out and no freeze-out are adopted for $T < T_{evap}$. In particular, constant H_2O abundances of $x(H_2O) = n(H_2O)/n(H_2) \sim 10^{-10}$, 10^{-8}, and 10^{-7} have been considered for the outer envelope where $T < T_{evap}$.

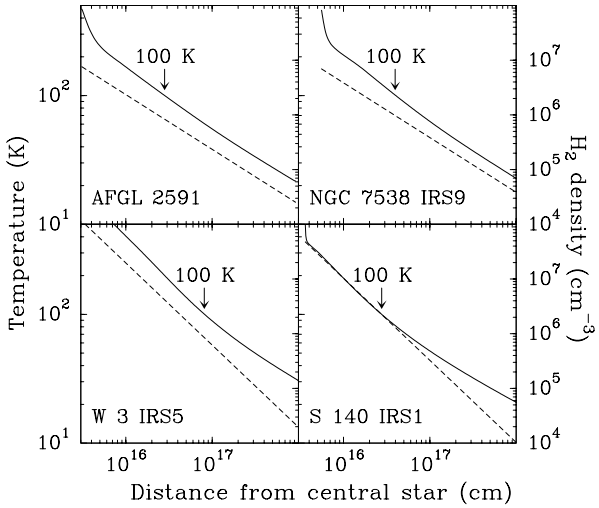

Fig. 3. Dust temperature (full lines) and density (dashed lines) profiles toward four of our sources.

In the following, we discuss one source, AFGL 2591, in detail to illustrate the methods and results, and then summarize more briefly the calculations for the other sources.

5. Results for AFGL 2591

5.1. Abundance profiles

For AFGL 2591 each of the 9 different chemical scenarios listed in Table 3 has been investigated. The resulting H_2O abundances as functions of position in the molecular envelope are shown in Fig. 4. In the case without ice evaporation (scenario 1), the H_2O abundance does not reach values of $\sim 10^{-4}$ until much closer to the central star than in the case of ice evaporation. This is due to the fact that high-temperature gas-phase chemistry does not produce high H_2O abundances until $T \gtrsim 230–300$ K while the evaporation of H_2O ice occurs around $T \sim 90–110$ K. When no freeze-out is included (scenarios 1 and 2) the abundances in the outer part of the molecular envelope can be as high as $\sim 10^{-6}$. Assuming different

Table 4. Comparison of predicted line fluxes[a] with the observed values for AFGL 2591.

Scenario	Transition and Wavelength					
	108.1 μm $2_{21}-1_{10}$	113.5 μm $4_{14}-3_{03}$	136.5 μm $3_{30}-3_{21}$	174.6 μm $3_{03}-2_{12}$	179.5 μm $2_{12}-1_{01}$	538.3 μm $1_{10}-1_{01}$
1	−5(−17)	1(−18)	9(−18)	2(−18)	−9(−18)	1.8
2	−6(−17)	8(−19)	1(−17)	2(−18)	−9(−18)	2.8
3	1(−17)	1(−17)	6(−18)	3(−18)	2(−18)	0.8
4	1(−18)	1(−17)	7(−18)	9(−19)	3(−19)	0.5
5	2(−17)	2(−17)	8(−18)	4(−18)	3(−18)	1.1
6	7(−18)	5(−18)	1(−18)	2(−18)	2(−18)	0.4
7	1(−17)	1(−17)	8(−18)	4(−18)	2(−18)	0.6
8	2(−18)	9(−18)	6(−18)	1(−18)	−3(−18)	0.5
9	−2(−17)	3(−18)	4(−18)	3(−18)	−6(−18)	0.6
Observed[b]	<−1.1(−17)[c]	<1.2(−17)	<8.3(−18)	<2.0(−17)	<2.9(−17)	0.37 ± 0.04

$a(b)$ means $a \times 10^b$.

[a] The line fluxes are given in W cm^{-2} μm^{-1}, except for the 538.3 μm line observed with SWAS, for which the integrated intensity in K km s^{-1} is listed. To convert to W cm^{-2}, multiply by $\Delta\lambda = \lambda/R$ in μm, with $R \approx 9200$. A negative value indicates absorption.

[b] The upper limits are 3σ values.

[c] Tentative detection at the 2.5σ level.

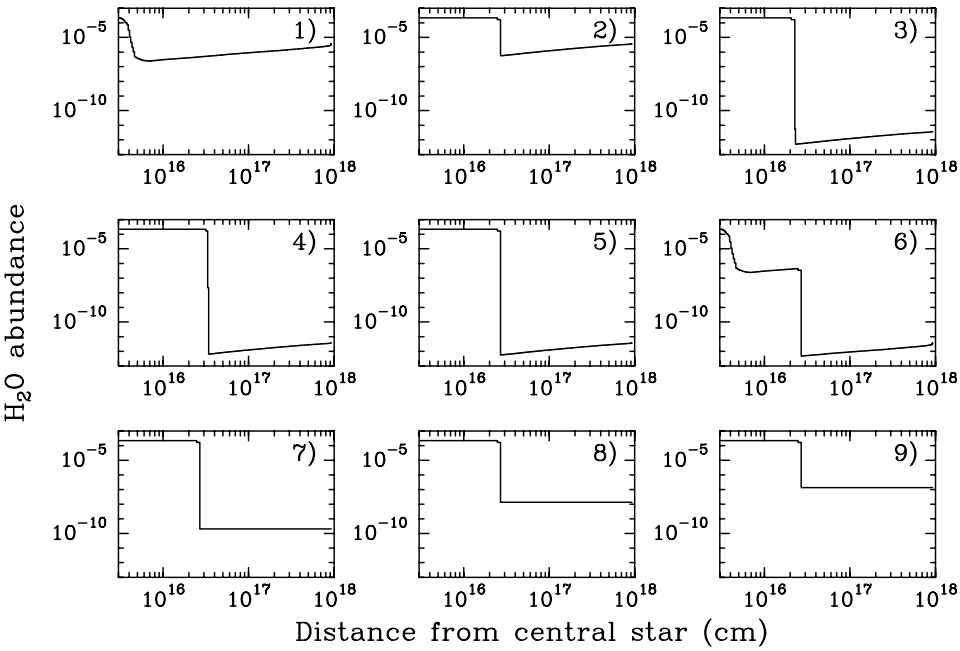

Fig. 4. H_2O abundances as functions of distance from the central star in the molecular envelope of AFGL 2591 for different chemical scenarios, using the physical structure for AFGL 2591 as derived by van der Tak et al. (2000b). The number in each panel refers to the scenario number in Table 3.

evaporation temperatures with similar thermal profiles as in Fig. 3 results in an H_2O abundance profile that reaches values of $\sim 10^{-4}$ at different points in the envelope (scenarios 3, 4, and 5). In the case of total or partial freeze-out, the H_2O abundances in the outer envelope are simply the adopted values (scenarios 3–9). Combining freeze-out with no ice evaporation results in an abundance profile that shows two jumps, one around $T \sim 230$–300 K when the high temperature chemistry drives most of the oxygen into H_2O and another around 100 K when freeze-out occurs (scenario 6). Between 100 and 230 K, ion-molecule gas-phase chemistry maintains a H_2O abundance of a few $\times 10^{-7}$.

5.2. Line fluxes

5.2.1. SWS results

The observed ro-vibrational spectrum of H_2O toward AFGL 2591 from Boonman & van Dishoeck (2003) is presented in Fig. 5. Modeling of the ro-vibrational band of H_2O

shows that the scenarios without ice evaporation (scenarios 1 and 6) cannot reproduce the observed spectrum: they have less H_2O at $T \sim 100-230$ K and simply do not have a large enough column of warm H_2O gas to produce deep enough absorptions. If an increased gas-phase H_2O abundance for $T \gtrsim 100$ K is adopted, simulating the effect of ice evaporation, the observed ro-vibrational H_2O band is well fit. Two representative model spectra with and without ice evaporation are shown in Fig. 5. The figure also shows the ratio of the differences between the SWS spectra and the two model spectra as a function of wavelength. This ratio is almost always higher than 1 and often higher than 1.5, demonstrating that the scenario with ice evaporation matches the observed data much better. This strengthens the conclusion based on the gas/solid ratio that ice evaporation is important for AFGL 2591 (Boonman & van Dishoeck 2003).

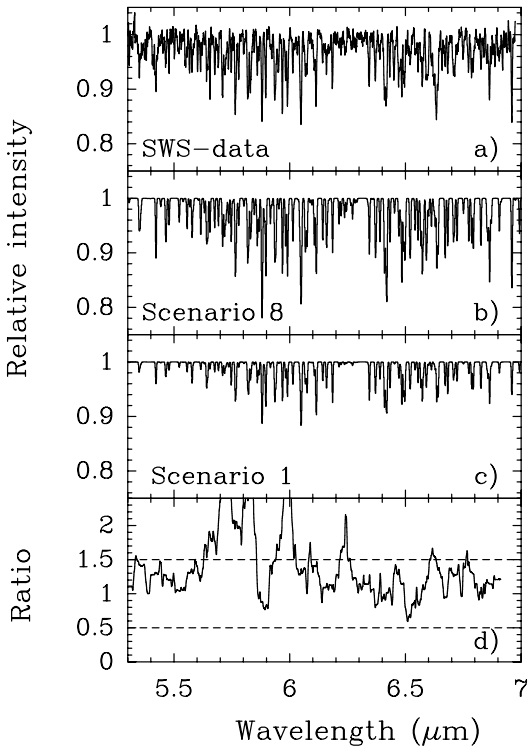

Fig. 5. a) The SWS data for the ν_2 ro-vibrational band in absorption toward AFGL 2591 as presented in Boonman & van Dishoeck (2003). **b)** Model spectrum based on chemical scenario 8, including ice evaporation and freeze-out. **c)** Model spectrum based on chemical scenario 1, without ice evaporation and without freeze-out. **d)** Ratio of the absolute differences between the model spectrum and the SWS data for panel **c)** and those for panel **b)**. This ratio demonstrates that the scenario with ice evaporation (scenario 8) matches the observations much better than that without ice evaporation (scenario 1) over almost the entire wavelength range.

5.2.2. LWS results

The predicted integrated intensities for the pure rotational H_2O lines as observed with LWS and SWAS are given in Table 4. This table shows that high H_2O abundances of $\gtrsim 10^{-8}$ in the cold gas (scenarios 1, 2 and 9) result in the prediction of the 108.1 μm and 179.5 μm lines in absorption. When less cold gas is present, the lines are calculated in emission. The $2_{12}-1_{01}$ line at 179.5 μm has the o-H_2O ground state as its lower level and therefore appears readily in absorption when any cold foreground gas is present. The H_2O $4_{14}-3_{03}$, $3_{30}-3_{21}$, and $3_{03}-2_{12}$ lines at 113.5, 136.5, and 174.6 μm respectively are always predicted to be in emission, with the 174.6 μm line not changing by more than a factor of ~4.5 for the different scenarios, probably due to its large optical depth ($\tau > 1000$), making it a poor diagnostic.

Comparison with the observational data shows that when no freeze-out is included (scenarios 1 and 2) the predicted absorption for the H_2O $2_{21}-1_{10}$ line at 108.1 μm is much deeper than the 2.5σ tentative detection. As a result, scenarios without freeze-out are not favored. Similarly scenario 5, which includes complete freeze-out, predicts fluxes for the 108.1 μm and 113 μm lines in emission that are somewhat higher than the 3σ noise levels. This also holds for the 108.1 μm line and scenario 9. Thus, neither scenario 5 nor 9 are preferred. The predicted fluxes for all other lines observed with LWS fall within the observed 3σ upper limits for all scenarios. However, scenarios 3 and 7 have several lines close to the 3σ upper limits, making these less likely than scenarios that predict lower values.

5.2.3. SWAS results

The predicted flux for the 557 GHz $1_{10}-1_{01}$ transition observed by SWAS is higher or equal to the observed integrated intensity for all scenarios (Table 4). However the observed value may be a lower limit, since the line profile suggests that absorption by a foreground cloud plays a role, which is not included in the model (Sect. 3). In that case, the actual integrated intensity could be a factor of up to ~2 larger than the value listed in Table 4.

Scenarios without freeze-out (scenarios 1 and 2) give too high intensities, even when taking the observed value to be twice as large. Also scenario 5 predicts a line flux that is too high. These results are consistent with the results for the LWS observations. The potential uncertainty in the observed integrated intensity makes it difficult to discriminate between scenarios with different degrees of freeze-out and evaporation at different temperatures (scenarios 6–9 versus 3–4).

Scenarios 3, 4, and 5 which have ice evaporation at 110 K, 90 K, and 100 K respectively, and total freeze-out below the evaporation temperature, show a variation in the predicted 557 GHz line flux with the evaporation temperature of a factor of ~2 (Table 4). The 557 GHz line is predicted to be highly optically thick ($\tau > 1000$) for these scenarios. Since thermalized emission from a region as large as the beam would give a much higher integrated intensity than observed, this indicates that the emission fills only a very small fraction of the beam. Therefore, the flux of the 557 GHz line is expected to increase with a decreasing evaporation temperature and consequently larger source size of the optically thick emission. However, the predicted fluxes for scenarios 3, 4, and 5 do not follow this trend for beam-filling, indicating that additional radiative transfer effects play a role. The differences in the model fluxes

suggest that the SWAS line is sensitive to the amount of warm gas at $T \sim 90-110$ K. On the other hand, the ro-vibrational H_2O lines observed with SWS are more sensitive to the hotter gas at $T > 110$ K, i.e. well above the temperature at which evaporation occurs (Fraser et al. 2001).

5.2.4. Combined SWS, LWS, and SWAS results

In order to quantify the quality of fit, the deviation of the predicted values for the different chemical scenarios from the observed values has been calculated separately for the SWS, LWS, and SWAS observations of gas-phase H_2O. For both the SWS and LWS data the deviation has been calculated using

$$\chi^2 = \frac{1}{N}\sum_i \left[\frac{F_i^{\rm model} - F_i^{\rm obs}}{\sigma_i}\right]^2, \quad (1)$$

where $F_i^{\rm obs}$ and $F_i^{\rm model}$ are the observed and predicted line fluxes, σ_i the one standard deviation noise level in the spectra for data point *i*, and the sum is taken over all *N* data points for the SWS observations and all *N* lines for the LWS observations. For the LWS observations $F^{\rm obs}$ is taken to be zero in case of a non-detection for which the observed 3σ noise levels are listed in Table 4. For all SWS data points σ_i is taken to be the 1σ noise level between 6.3 and 6.35 μm, which is relatively free from H_2O lines. For the SWAS observations the standard deviation ($\sqrt{\chi^2}$) is calculated, assigning a negative sign whenever the model prediction is lower than the observed value. Since only one line has been observed with SWAS, $N = 1$ in this case and for σ the uncertainty in the integrated intensity is adopted, which is taken to be 10% (Sect. 2.3).

Figure 6 shows the resulting χ^2 for the SWS and LWS lines and the $\sqrt{\chi^2}$ for the 557 GHz line for the nine different scenarios. It is seen that the LWS and SWAS data show the same trend, suggesting they probe at least partly the same gas. The calculated χ^2 for the ro-vibrational H_2O lines observed with SWS confirm the conclusion that ice evaporation plays an important role in AFGL 2591. In addition it shows that the SWS observations cannot distinguish between total or partial freeze-out, since the χ^2 does not change by more than 3% for scenarios including ice evaporation and at least some freeze-out (Fig. 6).

The minimum for all three types of observations (SWS, LWS, and SWAS) occurs for scenario 9, but this scenario predicts a deeper absorption for the H_2O $2_{21}-1_{10}$ line than the observed 2.5σ tentative feature. This effect is not taken into account in the calculation of the χ^2. The results from the previous sections already indicated that also scenarios 1, 2, 5, and 6 are not favored. The χ^2 results are in agreement with this and indicate that scenario 8 explains all three types of observations best. Scenario 8 has a total H_2O abundance of $\sim 2\times10^{-8}$ in the outer envelope, in good agreement with the results by Snell et al. (2000). This coincidence may be somewhat fortuitous, since Snell et al. (2000) use a much more simple radiative transfer model with a constant density and temperature throughout the envelope. Although it should be noted that the difference between scenario 8 and 4 is not significant, we will use scenario 8 as the preferred scenario.

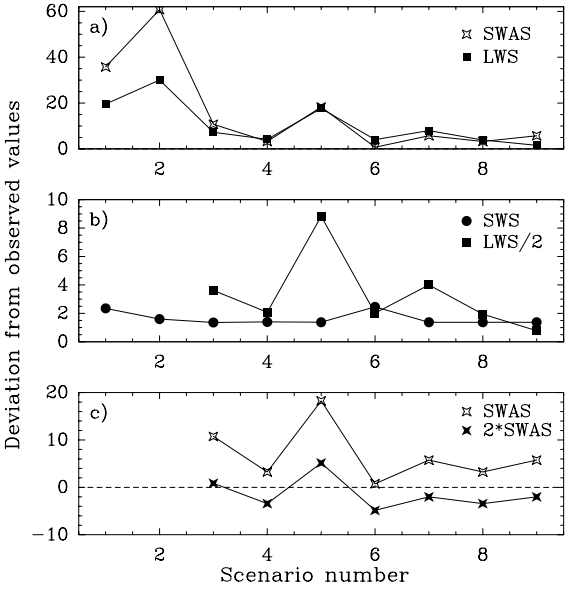

Fig. 6. Comparison of the predicted values for the different chemical scenarios with the observed values for AFGL 2591 (Table 4). For the ISO-SWS and -LWS data the χ^2 is presented, whereas for the SWAS data the signed standard deviation is shown (see text). The minimum absolute deviation corresponds to the chemical scenario that reproduces all observed H_2O lines best. **a)** Comparison of the deviation for the LWS and SWAS data. **b)** The deviation for the SWS data compared to a blow-up of that for the LWS data for scenarios 3–9. The LWS data have been divided by 2. **c)** Blow-up of the deviation for the SWAS data shown in panel **a)** for scenarios 3–9 compared to the deviation in case the observed SWAS line flux is a factor of 2 higher (filled stars).

5.2.5. Other chemical scenarios

To further investigate the possible sensitivity of the 557 GHz line to the chemical structure, a scenario similar to the preferred scenario 8, but with no warm H_2O gas in the inner envelope at $T > 100$ K, is investigated. This results in an integrated intensity of 0.2 K km s^{-1} for the 557 GHz line, a factor of 2.5 lower than for scenario 8. This provides further evidence for the suggestion that the 557 GHz line does not only probe cold H_2O gas in the outer envelope but is also sensitive to the warm inner gas, even in the large SWAS beam.

The scenarios discussed so far assume that evaporation and freeze-out occur instantaneously. The laboratory work by Fraser et al. (2001) shows that for evaporation this is likely to be the case for $T \gtrsim 110$ K and for freeze-out for $T \lesssim 90$ K. Therefore an additional scenario, including evaporation for $T \geq 110$ K, complete freeze-out for $T \leq 90$ K, and ion-molecule gas-phase chemistry between those temperatures has been explored. This scenario simulates non-instantaneous evaporation of H_2O ice. The resulting χ^2 for the SWS observations is comparable to those for scenarios with ice evaporation discussed before. The χ^2 for the LWS observations improves to 2.1 compared with 3.9 for our preferred scenario 8. The 557 GHz line is predicted to be 0.3 K km s^{-1}, close to the observed value of 0.37 K km s^{-1}, but lower than the corrected value taking into account the possibility of foreground absorption.

Thus, the case of non-instantaneous ice evaporation with complete freeze-out in the outer envelope can reproduce the SWS and LWS data as well or better than the case of instantaneous ice evaporation with partial freeze-out. However, the acceptance of the non-instantaneous ice evaporation model also requires that there be no foreground absorption of the SWAS 557 GHz line. If there is significant foreground absorption, scenario 8 with instantaneous evaporation and partial freeze-out in the outer envelope is preferred. It should be noted that there may be additional chemical scenarios, e.g. with a different gas-phase H_2O abundance above the evaporation temperature, that can explain the observed fluxes.

5.2.6. Effect of line width and emission

The above results have been derived using a Doppler b parameter of 2 km s^{-1} for the calculation of the level populations of H_2O and the integrated intensities of the pure rotational lines with the ALI model, and using b = 5 km s^{-1} for the calculation of the ro-vibrational spectrum. Using b = 2 km s^{-1} for the ro-vibrational lines significantly increases the calculated χ^2 value. Using b = 5 km s^{-1} in both the ALI model and the calculation of the ro-vibrational spectrum makes only small differences. Since the results for the different chemical scenarios show that the ro-vibrational lines probe warmer, and thus probably more turbulent, gas than the pure rotational lines, their line widths may be larger. A Doppler b value of 2 km s^{-1} is relevant for the cold gas, inferred from the $C^{34}S$ and $C^{17}O$ lines observed by van der Tak et al. (2000b), which probe the same cooler gas as the pure rotational H_2O lines.

In the calculations of the ro-vibrational spectrum it has been assumed that only absorption takes place. Including emission along the line of sight using the method described in Boonman & van Dishoeck (2003) does not result in a significantly higher χ^2 for the ro-vibrational lines observed with ISO-SWS, and thus does not change the above conclusions.

5.2.7. Other physical models

The adopted model for AFGL 2591 derived by van der Tak et al. (2000b) has an inner radius of ~200 AU, where the dust temperature is 440 K. Extending the density profile further inwards increases the χ^2 for the ro-vibrational band around 6 μm, but does not change the results significantly for the pure rotational lines observed with LWS. This is expected, since in this case only the amount of hot gas is increased, affecting only those lines which probe the warmest gas.

Assuming the $n \sim r^{-2}$ density power law from Doty & Neufeld (1997) throughout the entire envelope instead of $n \sim r^{-1}$, gives 108.1 and 113.5 μm lines for scenario 4 that are about 8 and 4 times stronger respectively in absorption than the observed upper limits. The ro-vibrational lines are predicted to be much stronger for this scenario, with a χ^2 about 5 times higher. The 557 GHz line is found to be 1.1 K km s^{-1}, also much stronger than the observed value. This is due to the fact that the total mass in the molecular envelope is kept the same, resulting in more warm H_2O gas and less cold H_2O gas for the steeper $n \sim r^{-2}$ density power law. Together these results suggest that a $n \sim r^{-2}$ density power law cannot explain the observed H_2O spectra for AFGL 2591. The ability to distinguish between different density power laws indicates that the chemistry can be used as a probe of the physical structure of the molecular envelopes of massive protostars, if it is well enough understood.

5.2.8. Summary

In summary, the SWS observations show that ice evaporation is important for AFGL 2591 in the inner envelope. Contrary to the results for the LWS lines, the SWS observations do not allow to distinguish between scenarios with different degrees of freeze-out in the outer part. The LWS observations rule out scenarios without freeze-out, and show that scenarios with cold gas-phase H_2O abundances of $<10^{-7}$ agree with the observed upper limits listed in Table 4. The calculated χ^2 for the LWS and SWAS data indicate the same trend with the chemical scenarios, suggesting these lines probe at least partly the same gas. Increasing the evaporation temperature from 90 to 110 K results in significant changes in the χ^2 for the pure rotational lines (Fig. 6), which cannot be explained by beam-filling effects for pure thermalized emission only. This indicates that these lines may be sensitive to gas at $T \sim$ 90–110 K, while the ro-vibrational lines observed with SWS are more sensitive to gas above the evaporation temperature. Combining the three different types of observations shows that scenario 8, with ice evaporation above 100 K and partial freeze-out at an abundance of $\sim 10^{-8}$ below 100 K is the preferred scenario.

6. Results for other sources

6.1. NGC 7538 IRS9

NGC 7538 IRS9 is the coldest source of the sample studied by van der Tak et al. (2000b) based on its observed spectral signatures. In particular, it has very deep ice absorption bands with no sign of ice heating (Gerakines et al. 1999; Boogert et al. 2000) and weak gas-phase lines with low gas/solid abundance ratios (Boonman & van Dishoeck 2003). It therefore forms a good contrast with AFGL 2591, which is among the warmest. For NGC 7538 IRS9, eight of the nine chemical scenarios (except scenario 7) have been investigated. The corresponding H_2O abundance profiles for this source show the same trends as for AFGL 2591. The main difference is that in the physical model for NGC 7538 IRS9 the evaporation temperature is reached at a larger distance from the source than in AFGL 2591, at $r \sim 3$–5×10^{16} cm for T = 90–110 K compared with $r \sim 2$–3×10^{16} cm for AFGL 2591. Overall, the size of the molecular envelope is a factor of ~2.5 larger for NGC 7538 IRS9 than for AFGL 2591, resulting in a larger fraction of cold gas than for AFGL 2591. The temperature of ~230–300 K above which most of the oxygen is driven into H_2O also occurs further outwards, at $r \sim 7 \times 10^{15}$ cm.

As for AFGL 2591, the deviation of the predicted values from the observed values has been calculated for the different chemical scenarios (see Sect. 5.2.4). The results are shown in

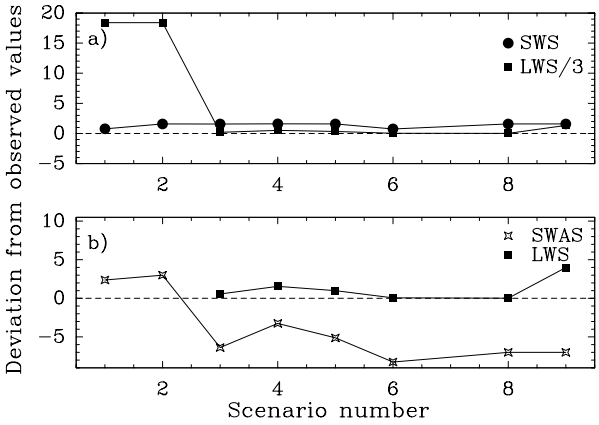

Fig. 7. Comparison of the predicted values for the different chemical scenarios with the observed values for NGC 7538 IRS9 (Table 5). For the SWS and LWS data the χ^2 is presented, whereas for the SWAS data the signed standard deviation is shown (see text). The minimum absolute deviation corresponds to the chemical scenario that reproduces all observed H_2O lines best. **a)** Comparison of the deviation for the LWS and SWS data. The LWS data have been divided by 3. **b)** The deviation for the SWAS data compared to a blow-up of that for the LWS data for scenarios 3–9. (Table 5).

Table 5. Line fluxes[a] for NGC 7538 IRS9.

	Transition and Wavelength			
Scenario	108.1 μm	174.6 μm	179.5 μm	538.3 μm
	$2_{21}-1_{10}$	$3_{03}-2_{12}$	$2_{12}-1_{01}$	$1_{10}-1_{01}$
1	−3(−17)	−9(−20)	−6(−18)	2.0
2	−3(−17)	3(−20)	−6(−18)	2.1
3	3(−18)	9(−19)	8(−19)	0.6
4	5(−18)	1(−18)	1(−18)	1.1
5	4(−18)	1(−18)	1(−18)	0.8
6	1(−18)	5(−19)	5(−19)	0.3
8	1(−19)	7(−19)	−2(−18)	0.5
9	−8(−18)	1(−18)	−4(−18)	0.5
Observed[b]	<7.0(−18)	<1.6(−17)	<3.0(−17)	1.62[c]

$a(b)$ means $a \times 10^b$.

[a] The line fluxes are given in W cm^{-2} μm^{-1}, except for the 538.3 μm line observed with SWAS, for which the integrated intensity in K km s^{-1} is listed. To convert to W cm^{-2}, multiply by $\Delta\lambda = \lambda/R$ in μm, with $R \approx 9200$. A negative value indicates absorption.

[b] The upper limits are 3σ values.

[c] This line likely contains contributions from the outflow, nearby sources, and/or a foreground cloud (see Sect. 3) and thus should be treated as an upper limit.

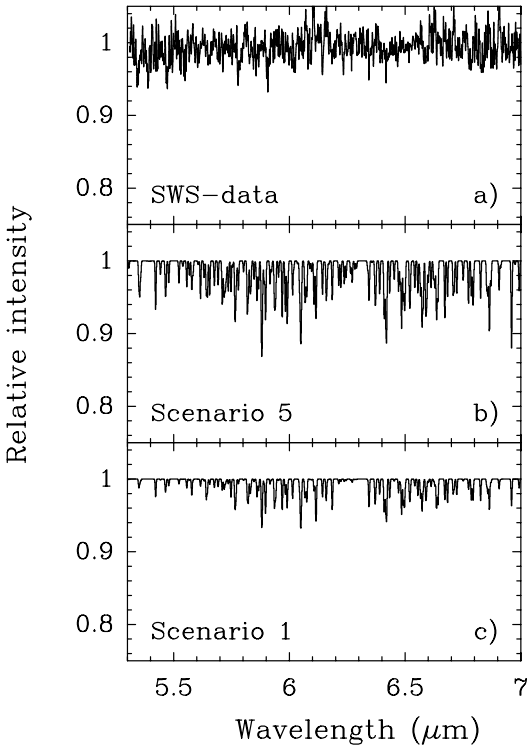

Fig. 8. a) The SWS spectrum toward NGC 7538 IRS9 as presented in Boonman & van Dishoeck (2003). **b)** Model spectrum based on chemical scenario 5, including ice evaporation and freeze-out (using b = 2.5 km s^{-1}). **c)** Model spectrum based on chemical scenario 1, without ice evaporation and without freeze-out (using b = 2.5 km s^{-1}).

Fig. 7. The χ^2 results for the SWS lines indicate that scenarios without ice evaporation can explain the observed ro-vibrational lines better than those with ice evaporation. This is illustrated in Fig. 8, which shows the non-detection of the ro-vibrational band of gas-phase H_2O toward NGC 7538 IRS9 as presented in Boonman & van Dishoeck (2003) along with two representative model spectra. Alternatively, it may indicate that the SWS data do not probe into the region where ice evaporation occurs for this source, perhaps due to optical depth effects at 6 μm, or that the inner envelope is not as warm as suggested by the adopted physical model, or H_2O may have been destroyed after evaporation, e.g. in a shock.

The pure rotational lines observed with LWS clearly prefer scenarios with a cold gas-phase H_2O abundance $<10^{-7}$ in the outer part, since the other scenarios predict too strong absorption for the $2_{21}-1_{10}$ 108.1 μm line compared to the observed upper limit (Table 5). However, the LWS lines cannot distinguish between the different degrees of freeze-out. As for AFGL 2591, the 108.1 and 179.5 μm lines change to emission when the amount of cold gas-phase H_2O decreases. All other scenarios with freeze-out give line fluxes smaller than the 3σ LWS upper limits and for the 174.6 and 179.5 μm lines even below the 1σ upper limits. The emission increases for all rotational lines when the evaporation temperature decreases and thus the size of the warm region increases. The increase is however small for the LWS lines, indicating that only some of these lines may be sensitive to the amount of gas between 90 and 110 K. The predicted integrated intensities for the observed pure rotational lines do not change by more than a factor of ∼5 between the different scenarios with total freeze-out. Except for scenarios without freeze-out, the 557 GHz line is always predicted too weak by a factor of $\gtrsim$1.5.

Combining the SWS and LWS results suggests that scenario 6 is the preferred scenario, but the SWAS results favor scenario 4. However, we prefer scenario 6, since the ∼4′ SWAS beam is much larger than that for the SWS observations, indicating that contamination by other sources can occur. Several

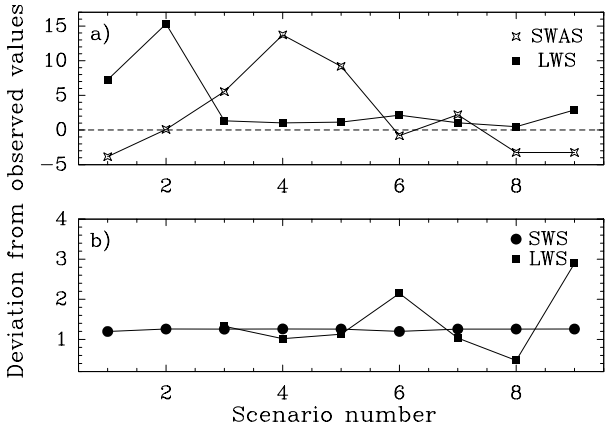

Fig. 9. Comparison of the predicted values for the different chemical scenarios with the observed values for W 3 IRS5 (Table 6). For the SWS and LWS data the χ^2 is presented, whereas for the SWAS data the signed standard deviation is shown (see text). The minimum absolute deviation corresponds to the chemical scenario that reproduces all observed H_2O lines best. **a)** Comparison of the deviation for the LWS and SWAS data. **b)** The deviation for the SWS data compared to a blow-up of that for the LWS data for scenarios 3–9.

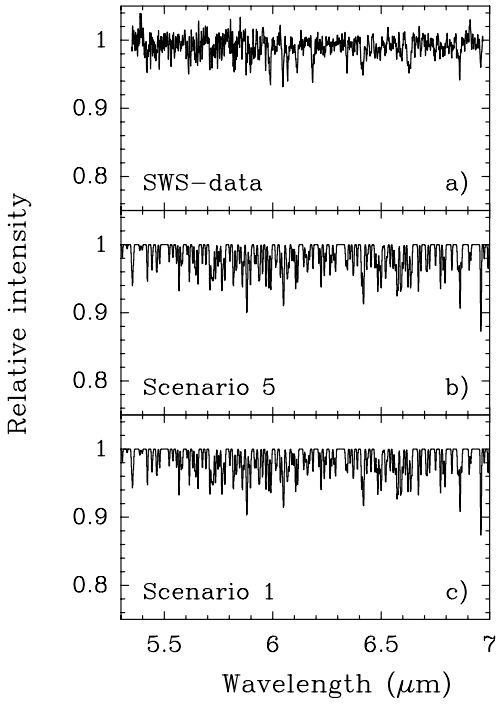

Fig. 10. a) The SWS spectrum toward W 3 IRS5 as presented in Boonman & van Dishoeck (2003). **b)** Model spectrum based on chemical scenario 5, including ice evaporation and freeze-out (using b = 1.5 km s^{-1}). **c)** Model spectrum based on chemical scenario 1, without ice evaporation and without freeze-out (using b = 1.5 km s^{-1}).

infrared sources are indeed located within the SWAS beam (e.g. Campbell & Persson 1988). Also, for NGC 7538 IRS9, the SWAS line has a contribution from the outflow and/or a foreground cloud which may amount to 60%, further suggesting that the observed integrated intensity for the H_2O $1_{10}-1_{01}$ 557 GHz line should be treated as an upper limit.

The above results have been calculated using a Doppler b value of 2.5 km s^{-1}, corresponding to the average line width of the rotational $C^{34}S$ and $C^{17}O$ lines observed by van der Tak et al. (2000b). Increasing b to 5 km s^{-1} for the ro-vibrational spectrum results in a significantly worse fit. Decreasing b to 1 km s^{-1} makes only small improvements in the χ^2 value.

6.2. W 3 IRS5

W 3 IRS5 is one of the most luminous sources in the sample of van der Tak et al. (2000b), located at a distance of ~2.2 kpc. Each of the nine different chemical scenarios has been investigated for W 3 IRS5. The total size of the envelope is similar to that of NGC 7538 IRS9, $r \sim 60\,000$ AU. Compared with AFGL 2591, the radius at which the temperature reaches ~230–300 K and the radius at which ice evaporation/freeze-out occurs, $r \sim 2 \times 10^{16}$ cm and $r \sim 6.5$–9×10^{16} cm respectively, are much further outwards. This results in a region of warm gas between ~100–300 K that is ~3–4 times larger than for AFGL 2591. The region of hot gas at $T \gtrsim 230$–300 K is also ~3–4 times larger than in AFGL 2591.

Figure 9 shows the deviation of the predicted values from the observed values for the different chemical scenarios (cf. Sect. 5.2.4). For the ro-vibrational band observed with SWS the calculated χ^2 changes only by a factor of ~1.05. This is illustrated in Fig. 10, which shows two representative model spectra along with the SWS observations. Thus, the importance of ice evaporation for W 3 IRS5 cannot be inferred from the SWS observations, unlike for AFGL 2591. This is probably caused by the much larger region with warm gas compared to that in AFGL 2591, producing a large enough warm H_2O column even without additional ice evaporation. The use of different b values or the inclusion of possible emission does not change this conclusion significantly, although the best fit is obtained for rather small line widths, $b \approx 1.5$ km s^{-1}, consistent with the $C^{34}S$ and $C^{17}O$ data.

The results for the pure rotational lines are presented in Table 6. Except for scenario 6, the 108.1 μm line is always predicted in absorption, in agreement with the tentative detection of this line. Scenarios without freeze-out (1 and 2) however predict a factor of ~3 too strong absorption. Besides the 108.1 μm line, several other lines, including those involving energy levels above 200 K, are in absorption for most scenarios. This is probably due to the large region of warm gas and dust in this source. Most of the predicted fluxes are consistent with the upper limits, except that scenario 2 predicts a line flux for the 113.5 μm line slightly higher than the 3σ limit. Scenario 9, with ice evaporation and a cold H_2O abundance of 10^{-7}, overpredicts the 108.1 μm line absorption by a factor of 2, whereas scenarios 3–6 with total freeze-out give a factor of >3 too low absorption. This suggests that partial freeze-out plays a role and that the H_2O abundance in the outer envelope is $<10^{-7}$.

All other pure rotational lines observed with LWS fall well below the observed 3σ upper limits and even below the 1σ upper limits for all scenarios with cold gas-phase abundances of $<10^{-7}$. The LWS lines do not show a clear trend for scenarios with and without ice evaporation.

Table 6. Line fluxes[a] for W 3 IRS5.

Scenario	Transition and Wavelength					
	108.1 μm $2_{21}-1_{10}$	113.5 μm $4_{14}-3_{03}$	136.5 μm $3_{30}-3_{21}$	174.6 μm $3_{03}-2_{12}$	179.5 μm $2_{12}-1_{01}$	538.3 μm $1_{10}-1_{01}$
1	−7(−17)	−2(−17)	−1(−17)	3(−18)	−1(−17)	2.0
2	−9(−17)	−3(−17)	1(−17)	−8(−19)	−2(−17)	3.3
3	−4(−18)	−2(−18)	4(−18)	8(−20)	−1(−18)	5.1
4	−8(−18)	−2(−18)	7(−18)	−3(−19)	−4(−18)	7.8
5	−6(−18)	−2(−18)	5(−18)	−7(−20)	−2(−18)	6.3
6	2(−18)	3(−18)	9(−19)	2(−18)	2(−18)	3.0
7	−7(−18)	−2(−18)	5(−18)	−4(−19)	−3(−18)	4.0
8	−2(−17)	−1(−17)	3(−18)	−2(−18)	−8(−18)	2.2
9	−5(−17)	−2(−17)	2(−18)	−3(−19)	−1(−17)	2.2
Observed[b]	<−2.5(−17)[c]	<2.9(−17)	<2.5(−17)	<2.1(−17)	<2.8(−17)	3.27 ± 0.33

$a(b)$ means $a \times 10^b$.

[a] The line fluxes are given in W cm^{-2} μm^{-1}, except for the 538.3 μm line observed with SWAS, for which the integrated intensity in K km s^{-1} is listed. To convert to W cm^{-2}, multiply by $\Delta\lambda = \lambda/R$ in μm, with $R \approx 9200$. A negative value indicates absorption.

[b] The upper limits are 3σ values.

[c] Tentative detection at the $\sim 3\sigma$ level, due to shifted wavelength of absorption feature (see Fig. 1).

The 557 GHz $1_{10}-1_{01}$ line observed by SWAS is best explained with scenarios 2 and 6. However, the above LWS results indicate that these two scenarios are not very likely. Scenarios with evaporation and total freeze-out predict integrated intensities that are higher than the observed value whereas the line becomes weaker when the evaporation/freeze-out temperature increases from 90 to 110 K, consistent with beam-filling effects only. A similar trend is also seen for the 108.1, 136.5 and 179.5 μm lines. The contribution of the outflow to the 557 GHz emission is estimated to be small for W 3 IRS5, but the presence of other sources in the beam may still result in an enhancement, so that the emission is treated as an upper limit. Recent ODIN observations of the 557 GHz line toward W 3 IRS5 by Wilson et al. (2003) show that some water emission is present beyond the 2.1′ ODIN beam. Therefore, of the scenarios that are in agreement with the LWS observations, scenario 8 explains the observed integrated intensity of the 557 GHz line best.

Unlike for AFGL 2591, the overall χ^2 values for the LWS lines do not follow the same trend as the SWAS line. This may suggest that in W 3 IRS5 some LWS lines probe different gas than the SWAS line. Combining the results for the three different types of observations shows that scenario 8, i.e., a model with ice evaporation in the inner part and with a low outer H_2O abundance, is the preferred scenario for W 3 IRS5.

6.3. S140 IRS1

Seven of the nine different chemical scenarios have been investigated for S 140 IRS1. This source is rather nearby at $d \approx 900$ pc, so that it fills a larger fraction of the LWS and SWAS beams. The size of this envelope is very similar to that of AFGL 2591, resulting in a similar distance from the central star at which evaporation occurs, $r \sim 2{-}3 \times 10^{16}$ cm for $T = 90$–110 K. The point at which the temperature reaches 230–300 K, $r \sim 7 \times 10^{15}$ cm, is also similar to that of AFGL 2591.

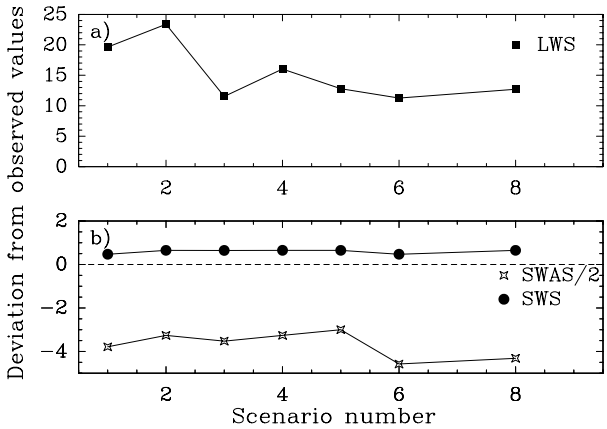

Fig. 11. Comparison of the predicted values for the different chemical scenarios with the observed values for S 140 IRS1 (Table 7). For the SWS and LWS data the χ^2 is presented, whereas for the SWAS data the signed standard deviation is shown (see text). The minimum absolute deviation corresponds to the chemical scenario that reproduces all observed H_2O lines best. **a)** The deviation for the LWS data. **b)** Comparison of the deviation for the SWS and SWAS data. The SWAS data have been divided by 2.

The deviations of the model values from the observed ones are shown in Fig. 11 for the different chemical scenarios. The χ^2 for the SWS data shows that scenarios without ice evaporation give somewhat better results. While most of the predicted lines in both scenarios are in agreement with the non-detection of ro-vibrational H_2O lines in this source, Fig. 12 shows that some lines are predicted stronger than the noise level in both cases. A slightly better fit to the data is obtained with $b = 1$ rather than 2 km s^{-1}, indicating that the intrinsic widths of the lines in this source are small.

The χ^2 values for the pure rotational lines observed with LWS are large for all scenarios, consistent with the predicted line fluxes listed in Table 7. In contrast with the other

Table 7. Line fluxes[a] for S140 IRS1.

Scenario	Transition and Wavelength				
	113.5 μm	136.5 μm	174.6 μm	179.5 μm	538.3 μm
	$4_{14}-3_{03}$	$3_{30}-3_{21}$	$3_{03}-2_{12}$	$2_{12}-1_{01}$	$1_{10}-1_{01}$
1	−7(−18)	1(−17)	9(−19)	−1(−17)	0.5
2	−1(−17)	1(−17)	−5(−19)	−1(−17)	0.7
3	3(−18)	3(−18)	2(−18)	9(−19)	0.6
4	6(−18)	8(−18)	2(−18)	−2(−19)	0.7
5	4(−18)	5(−18)	2(−18)	9(−19)	0.8
6	−3(−19)	8(−19)	7(−19)	1(−18)	0.2
8	−3(−18)	3(−18)	2(−20)	−6(−18)	0.3
Observed[b]	<6.2(−18)	<6.5(−18)	4.2(−17)	<2.6(−17)	1.94

$a(b)$ means $a \times 10^b$.

[a] The line fluxes are given in W cm^{-2} μm^{-1}, except for the 538.3 μm line observed with SWAS, for which the integrated intensity in K km s^{-1} is listed. To convert to W cm^{-2}, multiply by $\Delta\lambda = \lambda/R$ in μm, with $R \approx 9200$. A negative value indicates absorption.

[b] The upper limits are 3σ values.

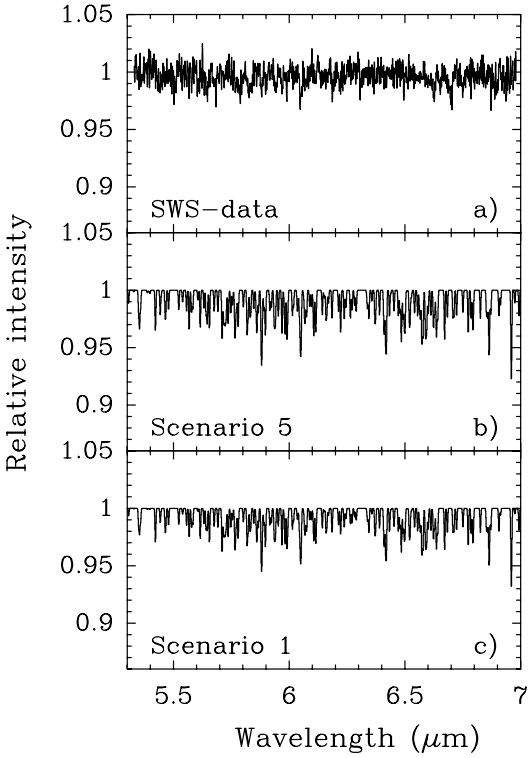

Fig. 12. a) The SWS spectrum toward S 140 IRS1 as presented in Boonman & van Dishoeck (2003). **b)** Model spectrum based on chemical scenario 5, including ice evaporation and freeze-out (using b = 1.0 km s^{-1}). **c)** Model spectrum based on chemical scenario 1, without ice evaporation and without freeze-out (using b = 1.0 km s^{-1}).

sources, the $3_{03}-2_{12}$ line at 174.6 μm is clearly detected in S 140 IRS1 in emission (see Fig. 1). None of the scenarios can explain this detection. The predicted fluxes for this line are a factor of >20 too low compared to the observed flux of 4.2×10^{-17} W cm^{-2} μm^{-1}. The integrated flux of the H_2O $3_{03}-2_{12}$ line is 2.0×10^{-18} W cm^{-2}. In addition, the 557 GHz line is also predicted a factor of >2 too low compared to the observed value for all scenarios. As for AFGL 2591, this line is sensitive not only to the cold outer envelope but also to the warm inner region where the ice evaporates. Scenarios 1 and 2 without freeze-out overpredict the observed upper limits for the 113.5 and 136.5 μm lines, suggesting that these scenarios are very unlikely. Scenario 4, with evaporation and complete freeze-out at 90 K, somewhat overpredicts the 136.5 μm line.

As for the other sources, the 108.1 and 179.5 μm lines are predicted in absorption when no freeze-out is included and turn to emission when the degree of freeze-out increases. The predictions for the 179.5 μm line are well below the observed upper limit for all scenarios.

Because of the large deviations for both the LWS and SWAS lines, a clear preferred scenario cannot be determined. Of the seven scenarios, scenarios 3, 5, and 6 are the best choices. This indicates that scenarios with freeze-out are preferred over those without.

Van der Tak et al. (2000b) note that S 140 IRS1 is different from the other sources discussed here, in that it is probably the only source for which the assumption of one central heating source breaks down. This is due to the presence of the sources IRS2 and IRS3 with luminosities comparable to that of IRS1 within a ∼10″–15″ offset, which is likely to influence the physical conditions in the envelope of IRS1. Therefore, some additional physical models have been investigated in which the luminosity is increased by factors of 3, 5, and 10 resulting in higher temperatures throughout the envelope. These models are combined with chemical scenario 5, resulting in χ^2 values for the LWS lines that are a factor of >2.5 higher compared to the original model with the same scenario. The model with a 10 times higher luminosity is the only one that can reproduce the detected H_2O $3_{03}-2_{12}$ emission line, but this model overpredicts the other LWS lines. The corresponding predictions for the 557 GHz line are however closer to the observed value. The fit to the SWS lines does not change significantly. Using scenario 8 instead of scenario 5 in combination with an increased luminosity gives similar results for both the LWS, SWAS, and SWS data. This indicates that increasing the luminosity helps

Table 8. Observed LWS line fluxes for NGC 7538 IRS1.

Wavelength	H_2O transition	Flux[a]
99.5 μm	$5_{05}-4_{14}$	<1.7(−17)
108.1 μm	$2_{21}-1_{10}$	<9.6(−18)
113.5 μm	$4_{14}-3_{03}$	<1.2(−17)
132.4 μm	$4_{23}-4_{14}$	<9.7(−18)[b]
138.5 μm	$3_{13}-2_{02}$	<1.6(−17)
174.6 μm	$3_{03}-2_{12}$	<1.0(−17)
179.5 μm	$2_{12}-1_{01}$	<1.9(−17)
180.5 μm	$2_{21}-2_{12}$	<1.4(−17)

$a(b)$ means $a \times 10^b$.

[a] Fluxes are in W cm^{-2} μm^{-1}. The upper limits are 3σ values. To convert to W cm^{-2}, multiply by $\Delta\lambda = \lambda/R$ in μm, with $R \approx 9200$.

[b] Tentative detection at the 3σ level, due to shifted wavelength of absorption feature.

explaining the SWAS line, as well as the $3_{03}-2_{12}$ 174.6 μm LWS line.

Van der Tak et al. (2000b) note that the dust in the envelope of S 140 IRS1 prefers a density gradient proportional to r^{-1}, whereas the gas follows a $r^{-1.5}$ density power law. Using the former density gradient in combination with scenario 5 and an increased luminosity gives similar results as for the $r^{-1.5}$ density power law. Thus, increasing the luminosity or changing the density gradient cannot explain the detected H_2O $3_{03}-2_{12}$ emission line and the observed upper limits for the other LWS lines simultaneously. Since the S 140 cloud is exposed to intense ultraviolet radiation, models which include additional external rather than internal heating are yet another alternative. Such models remain to be investigated.

6.4. NGC 7538 IRS1 and MonR2 IRS3

MonR2 IRS3 and NGC 7538 IRS1 have not been modeled in as great detail as the other sources. However, NGC 7538 IRS1 has a similar density gradient as NGC 7538 IRS9 and also a similar envelope size (van der Tak et al. 2000b). In addition, the SWS spectrum is very similar to that of NGC 7538 IRS9 with little or no H_2O absorption seen. This may indicate that NGC 7538 IRS1 has either very high optical depth at 6 μm or small line widths, hiding the presence of abundant H_2O, or that ice evaporation is not important. Using the H_2O ice column density from Gerakines et al. (1999), an H_2O ice abundance of $\sim 7 \times 10^{-5}$ is found for this source, much lower than that toward IRS9. This suggests that the latter explanation is not very likely (see also Boonman & van Dishoeck 2003). Comparison of the observed values for the NGC 7538 IRS1 LWS (Table 8) and SWAS (Table 2) lines with the predicted fluxes for the NGC 7538 IRS9 models in Table 5 shows that the LWS data rule out scenarios without freeze-out. As for IRS 9, the 557 GHz SWAS line cannot be reproduced, but this may be partly due to a contribution from the outflow, emission from a foreground cloud, and/or additional sources to the observed line. Since the bolometric luminosity of NGC 7538 IRS1 is a factor of three higher than that of NGC 7538 IRS9, comparison with W 3 IRS5 may be more appropiate. Comparing Tables 8 and 6 shows that the LWS data rule out scenarios with cold gas-phase H_2O abundances $>10^{-8}$.

Van der Tak et al. (2003) derive a $r^{-1.25}$ density power-law for MonR2 IRS3, in between those of AFGL 2591 and NGC 7538 IRS9 on one side, and W 3 IRS5 and S 140 IRS1 on the other side. Like AFGL 2591, the SWS spectrum toward MonR2 IRS3 shows the presence of many ro-vibrational gas-phase H_2O lines, with a depth in between those of AFGL 2591 and W 3 IRS5. Since the results for these two sources indicate that ice evaporation is important, it is expected that this also holds for MonR2 IRS3. The inferred H_2O gas/solid ratio indicates this as well (see Boonman & van Dishoeck 2003). The observed integrated intensity of 1.91 K km s^{-1} for the 557 GHz SWAS line also falls in between those for AFGL 2591 and W 3 IRS5, and is comparable to that of S 140 IRS1. No LWS data are available for MonR2 IRS3. This makes it difficult to investigate the importance of freeze-out, since the SWAS line may be contaminated by the presence of nearby infrared sources and has an outflow contribution.

7. Discussion

7.1. Comparison of sources

Table 9 summarizes the chemical scenario for each source that explains best the SWS, LWS, and SWAS observations. It shows that freeze-out is important in the outer envelope for all sources, which is mainly determined from the LWS observations, but the degree seems to vary between sources. The observations do not allow an accurate determination of the abundance of the remaining cold gas-phase H_2O, but it is certainly small compared with that in the ice mantles, <0.1%. Theoretical models indeed predict that some residual H_2O can be maintained in the gas-phase after freeze-out through cosmic-ray removal of oxygen (Bergin et al. 2000). While the low gas-phase H_2O abundances in the cold outer envelope have already been suggested on the basis of a simple analysis by Snell et al. (2000) from SWAS observations only, the more detailed modeling presented here shows that the 557 GHz line is also sensitive to gas around $T \sim 90$–110 K. Thus, it probes not only the cold molecular envelope, even with the large SWAS beam. This conclusion of course assumes that the observed 557 GHz line is not contaminated or overwhelmed by outflow emission or emission from other sources in the beam.

Ice evaporation appears to be important for all sources except NGC 7538 IRS9 (Table 9). This confirms the earlier result from gas/solid ratios based on a more simple analysis (van Dishoeck 1998; Boonman & van Dishoeck 2003). The accuracy of the observations does not allow to determine the precise evaporation temperature. However, the results found in this paper are consistent with the experimental results that evaporation takes place between ~90–110 K (Fraser et al. 2001). The importance of ice evaporation is mainly derived from the ro-vibrational SWS spectra. As noted above, the lack of H_2O absorption toward NGC 7538 IRS9 may be an optical depth and/or geometrical effect, or H_2O may have been destroyed after evaporation. For AFGL 2591 which shows the strongest

Table 9. Preferred chemical scenarios for the different sources[a].

Source	Ice evaporation	Freeze-out	Cold gas-phase H_2O	$N(H_2O_{ice})$[b]	$T_{ex}(C_2H_2)$[c] (K)
AFGL 2591	YES, $T \sim$ 90–110 K	YES, $T \lesssim$ 90–110 K	$x(H_2O) \sim 0$–10^{-8}	1.7(18)	900
NGC 7538 IRS1	YES	YES, $T \lesssim$ 90–110 K	$x(H_2O) \lesssim 10^{-8}$	3.1(18)	500
W 3 IRS5	YES, $T \sim$ 90–110 K	YES, $T \lesssim$ 90–110 K	$x(H_2O) \lesssim 10^{-8}$	5.1(18)	500
S 140 IRS1	?	YES, $T \lesssim$ 100 K	$x(H_2O) \sim 0$	2.0(18)	390
MonR2 IRS3	YES, $T \sim$ 90–110 K	?	?	1.9(18)	310
NGC 7538 IRS9	NO	YES, $T \lesssim$ 100 K	$x(H_2O) \sim 0$	7.0(18)	300

$a(b)$ means $a \times 10^b$.

[a] The sources are ordered by a decreasing temperature of the warm gas (Lahuis & van Dishoeck 2000).

[b] H_2O ice column densities from Gibb & Whittet (2002). H_2O ice column density for AFGL 2591 from Smith et al. (1989) and for NGC 7538 IRS1 from Gerakines et al. (1999).

[c] C_2H_2 excitation temperature from Lahuis & van Dishoeck (2000) and Boonman et al. (2003), which is a good tracer of the warm gas. For MonR2 IRS3 and S 140 IRS1 the ^{13}CO temperatures from Giannakopoulou et al. (1997) and Mitchell et al. (1990) respectively, are listed.

H_2O absorption, the line of sight passes close to the molecular outflow which may decrease the optical depth along the line of sight, enabling a deeper look into the molecular envelope and thus probe hotter gas (van der Tak et al. 1999). This could also explain the larger line widths found for the ro-vibrational lines in AFGL 2591 compared to the other sources, which have more collimated outflows.

In Table 9 the sources are ordered by a decreasing temperature of the molecular envelope, using different temperature tracers. As shown by van der Tak et al. (2000b), lower temperatures may be related to less dispersion of the envelope. In this scenario, AFGL 2591 is the most evolved object and NGC 7538 IRS9 is one of the youngest.

7.2. H_2O ice

The models indicate that freeze out of H_2O and its precursors in the outer envelope is significant. It is assumed that most oxygen frozen out on grains is converted to H_2O ice. Is this consistent with the observed ice columns toward the sources? The observed values are listed in Table 9 (Keane et al. 2001; Smith et al. 1989; Gibb & Whittet 2002), and show that the amount of H_2O ice along the line of sight decreases with increased heating of the envelope. As stated in the previous section, no sign of ice evaporation is seen toward NGC 7538 IRS9, consistent with its large observed H_2O ice column density. This provides additional evidence for the cold nature of this source, which has been inferred from other observations as well (e.g. Boogert et al. 2000; Gerakines et al. 1999).

The H_2O ice column density in the outer envelope below the evaporation temperature can be calculated using the temperature and density profiles in Fig. 3 and an adopted H_2O ice abundance of 2×10^{-4} with respect to H_2 (Sect. 4.1). The results show that the difference between evaporation at $T = 90$ K and 110 K is less than 30% for all sources, which is not enough to distinguish them. The modeled H_2O ice column densities are higher by a factor of ~3–6. This discrepancy may have several reasons. For example, the outer radius of the envelope may be too large, making the modeled H_2O ice column too high. Van der Tak et al. (2000b) state that the outer radius in their models is twice the radius of the CS emission used to derive the density profiles. Using an outer radius equal to that of the CS emission reduces the modeled H_2O ice column by a factor of ~1.1–1.3, not sufficient by itself to explain the discrepancy. Alternatively, not all oxygen may be converted into H_2O ice. In particular, at high densities less atomic H is available to convert atomic O into H_2O on grains (Tielens 1989), or atomic oxygen may be locked-up in the grain core.

Combined, these effects may be sufficient to explain a factor of a few difference between the observed and modeled values, indicating that the presented models are not in disagreement with the H_2O ice observations.

7.3. Shocks

The models discussed in this paper consider only quiescent chemistry. However, all of our sources possess an outflow. This leads to the question to what extent shocks are important for the production of H_2O in these sources, especially on the larger scales probed by the LWS and SWAS lines. In Sect. 3, the contribution of the outflow to the SWAS 557 GHz line has been determined from fits to the narrow and broad components (Fig. 2). Since neither the SWS nor the LWS lines are spectrally resolved, such a decomposition cannot be performed for higher excitation lines.

A study of sulphur-bearing species toward the same objects shows that both shock models and models with ice evaporation can explain the observations (van der Tak et al. 2003). The low inferred abundances of gas-phase CO_2 below $T \sim 300$ K toward these sources (Boonman et al. 2003) have been interpreted by destruction by shocks (Charnley & Kaufman 2000). In a shock with a sufficiently high H/H_2 ratio the evaporated H_2O will also be destroyed. Both CO_2 and H_2O may reform in the warm postshock gas. If freeze-out in the colder envelope is not instantaneous, this may provide an alternative explanation for the presence of partial freeze-out in some of our sources.

In order to see the potential observational effect of shocks, an Orion-type shock at the distance of our sources has been considered. Using the model by Kaufman & Neufeld (1996), gives H_2O line fluxes a factor of ~100 larger than the observed

upper limits in the case of AFGL 2591. This indicates that such a strong shock would have dominated the LWS spectra, contrary to what is observed. Even at the distance of SgrB2, such a shock could be detected. The absence of such shocks for any of our high-mass sources indicates that they fill at most a few percent of the LWS beam and thus of the envelope. Alternatively, it suggests the absence of shocks with velocities greater than $\sim$15 km s^{-1}.

Regardless of the precise contribution from shocks, some fraction of the observed emission must result from warm H_2O in the inner envelope produced by ice evaporation. Van der Tak et al. (2000a) have shown that the CH_3OH line profiles toward the sources discussed in this paper do not show evidence for an outflow component. Consequently, the high inferred CH_3OH abundances result from evaporation of ices due to thermal heating, and similar conclusions likely hold for other molecules.

7.4. Future prospects

Among the rotational lines observed with ISO-LWS and SWAS and studied here are three transitions that can also be observed with the Heterodyne Instrument for the Far-Infrared (HIFI) on board Herschel. These are the $3_{03}-2_{12}$, $2_{12}-1_{01}$, and $1_{10}-1_{01}$ lines at 174.6, 179.5, and 538.3 μm (557 GHz) respectively. Comparing the predicted line fluxes for these lines in Tables 4–7 shows that the $3_{03}-2_{12}$ line is never predicted stronger than 4×10^{-18} W cm^{-2} μm^{-1}, corresponding to an integrated intensity of $\sim8\times10^{-20}$ W cm^{-2}. For all sources except W 3 IRS5 this line is predicted mostly in emission. This suggests that beam dilution plays a role for this line in the large LWS beam of $\sim$80″, which is about $\sim$6 times larger than the HIFI beam at the same frequency. The $3_{03}-2_{12}$ line is the only LWS line detected toward one of our sources, S 140 IRS1, with a strength of 4.2×10^{-17} W cm^{-2} μm^{-1} and an integrated intensity of $\sim2\times10^{-18}$ W cm^{-2}. Since the upper level of this line arises from an energy level of $\sim$197 K, this will be a useful transition to study the warm H_2O gas in massive protostars in more detail, in particular the kinematics with the much higher spectral resolution of HIFI compared to ISO.

The $2_{12}-1_{01}$ 179.5 μm line, which connects with the o–H_2O ground state, is predicted to be strongly in absorption whenever there is some cold gas-phase H_2O present. With the higher spectral resolution of HIFI, the absorptions will be much deeper so that this line will be very suitable to study the effects of freeze-out in the molecular envelopes of massive protostars. In addition, the $3_{03}-2_{12}$ and $2_{12}-1_{01}$ lines have one level in common at $E\sim115$ K. If both lines are detected in emission it is likely that they both originate in gas above the evaporation temperature of H_2O ice. In that case, the combination of these two lines can tell more about the excitation temperature of the gas in which they originate. If the $2_{12}-1_{01}$ line is detected in absorption, it will probe much colder gas. The combination with the $3_{03}-2_{12}$ line will then provide information on the differences and/or similarities of the cold versus the warm H_2O gas, e.g., the kinematics.

As shown in the previous sections, the 557 GHz line is also sensitive to both the cold and the warm gas in the envelope. Observations of this line with HIFI in a much smaller beam of $\sim$39″ compared with SWAS will be important to solve problems of contamination by other sources or surrounding clouds, e.g. by observations toward the source center and at different off-positions.

8. Conclusions

Observations of H_2O toward a set of deeply embedded massive protostars have been presented, using three different observational techniques. A radiative transfer model has been used for comparison of observed H_2O lines with different chemical scenarios, in order to probe the chemical structure of their envelopes. The main conclusions are as follows.

- Pure gas-phase production of H_2O cannot explain the observed spectra between $\sim$5 and 540 μm in the 6 deeply embedded massive protostars studied.
- Freeze-out in the cold outer envelope is important for all sources, as indicated by the ISO-LWS results. The detailed modeling in this paper thus confirms the earlier results from the 557 GHz line observed with SWAS that the gas-phase H_2O abundances in the cold outer envelope of our sources are low. The observations do not allow an accurate determination of the degree of freeze-out, resulting in cold gas-phase H_2O abundances that can easily differ by more than an order of magnitude, but are likely $\lesssim10^{-8}$.
- Our models indicate that the 557 GHz SWAS line does not only probe the cold outer parts of the molecular envelope, but includes an important contribution from warm H_2O gas around the evaporation temperature of $T\sim$ 90–110 K.
- Ice evaporation is important for all sources except maybe NGC 7538 IRS9, as shown by the ISO-SWS data. The accuracy of the observations does not allow a determination of the evaporation temperature, but values between $T\sim$ 90–110 K, found from laboratory experiments, are consistent with the data.
- Shocks do not seem to be a dominant production mechanism of gas-phase H_2O for the deeply embedded massive protostars studied here.
- At present, the detected H_2O $3_{03}-2_{12}$ emission line toward S 140 IRS1 and the observed upper limits for the other LWS lines cannot be explained simultaneously. Further modeling, for example using a clumpy envelope model heated from the outside, is needed to investigate the physical and chemical conditions in this source. The SWAS data for S 140 IRS1 can be explained by using an increased luminosity.
- The model results show that the $3_{03}-2_{12}$, $2_{12}-1_{01}$, and $1_{10}-1_{01}$ lines are good candidates for HIFI on board Herschel to provide important chemical information, such as the degree of freeze-out in the outer envelope and the relative importance of thermal evaporation and shocks in the inner part.

Acknowledgements. This work was partially supported by a grant from The Research Corporation (SDD), by the NWO grant

614-41-003, and by a NWO Spinoza grant. The authors wish to thank Floris van der Tak, Xander Tielens, and Gerd-Jan van Zadelhoff for useful discussions.

References

Ashby, M. L. N., Bergin, E. A., Plume, R., et al. 2000, ApJ, 539, L119

Bergin, E. A., Neufeld, D. A., & Melnick, G. J. 1998, ApJ, 499, 777

Bergin, E. A., Melnick, G. J., Stauffer, J. R., et al. 2000, ApJ, 539, L129

Boogert, A. C. A., Ehrenfreund, P., Gerakines, P. A., et al. 2000, A&A, 353, 349

Boonman, A. M. S., van Dishoeck, E. F., Lahuis, F., Wright, C. M., & Doty, S. D. 2000, in ISO beyond the Peaks, ESA-SP, 456, 67 [astro-ph/0105249]

Boonman, A. M. S., Stark, R., van der Tak, F. F. S., et al. 2001, ApJ, 553, L63

Boonman, A. M. S., & van Dishoeck, E. F. 2003, A&A, 403, 1003

Boonman, A. M. S., van Dishoeck, E. F., Lahuis, F., & Doty, S. D. 2003, A&A, 399, 1063

Campbell, B., & Persson, S. E. 1988, AJ, 95, 1185

Cernicharo, J., Lim, T., Cox, P., et al. 1997, A&A, 323, L25

Cernicharo, J., Perez-Martinez, S., González-Alfonso, E., et al. 1999, in The Universe as Seen by ISO, ed. P. Cox, & M. F. Kessler, ESA-SP, 427, 651

Ceccarelli, C., Caux, E., Loinard, L., et al. 1999, A&A, 342, L21

Charnley, S. B. 1997, ApJ, 481, 396

Charnley, S. B., & Kaufman, M. J. 2000, ApJ, 529, L111

Doty, S. D., & Neufeld, D. A. 1997, ApJ, 489, 122

Doty, S. D., van Dishoeck, E. F., van der Tak, F. F. S., & Boonman, A. M. S. 2002, A&A, 389, 446

Draine, B. T., Roberge, W. G., & Dalgarno, A. 1983, ApJ, 264, 485

Ehrenfreund, P., Dartois, E., Demyk, K., & d'Hendecourt, L. 1998, A&A, 339, L17

Fraser, H. J., Collings, M. P., McCoustra, M. R. S., & Williams, D. A. 2001, MNRAS, 327, 1165

Gerakines, P. A., Whittet, D. C. B., Ehrenfreund, P., et al. 1999, ApJ, 522, 357

Giannakopoulou, J., Mitchell, G. F., Hasegawa, T. I., Matthews, H. E., Maillard, J.-P. 1997, ApJ, 487, 346

Gibb, E. L., & Whittet, D. C. B. 2002, ApJ, 566, L113

González-Alfonso, E., Cernicharo, J., van Dishoeck, E. F., Wright, C. M., & Heras, A. 1998, ApJ, 502, L169

Green, S., Maluendes, S., & McLean, A. D. 1993, ApJS, 85, 181

Harwit, M., Neufeld, D. A., Melnick, G. J., & Kaufman, M. J. 1998, ApJ, 497, L105

Helmich, F. P., van Dishoeck, E. F., Black, J. H., et al. 1996, A&A, 315, L173

Hollenbach, D., & McKee, C. F. 1979, ApJS, 41, 555

Kaufman, M. J., & Neufeld, D. A. 1996, ApJ, 456, 611

Keane, J. V., Tielens, A. G. G. M., Boogert, A. C. A., Schutte, W. A., & Whittet, D. C. B. 2001, A&A, 376, 254

Lahuis, F., & van Dishoeck, E. F. 2000, A&A, 355, 699

Lee, H.-H., Bettens, R. P. A., & Herbst, E. 1996, A&AS, 119, 111

Le Teuff, Y. H., Millar, T. J., & Markwick, A. J. 2000, A&AS, 146, 157

Melnick, G. J., Stauffer, J. R., Ashby, M. L. N., et al. 2000a, ApJ, 539, L77

Melnick, G. J., Ashby, M. L. N., Plume, R., et al. 2000b, ApJ, 539, L87

Mitchell, G. F., Maillard, J.-P., Allen, M., Beer, R., & Belcourt, K. 1990, ApJ, 363, 554

Mitchell, G. F., & Hasegawa, T. I. 1991, ApJ, 371, L33

Mitchell, G. F., Hasegawa, T. I., & Schella, J. 1992, ApJ, 386, 604

Nisini, B., Benedettini, M., Giannini, T., et al. 1999, A&A, 350, 529

Nisini, B., Giannini, T., & Lorenzetti, D. 2002, ApJ, 574, 246

Phillips, T. R., & Green, S. 1995, Ap&SS, 224, 537

Skinner, C. J., Tielens, A. G. G. M., Barlow, M. J., & Justtanont, K. 1992, ApJ, 399, L79

Smith, R. G., Sellgren, K., & Tokunaga, A. T. 1989, ApJ, 344, 413

Snell, R. L., Howe, J. E., Ashby, M. L. N., et al. 2000, ApJ, 539, L101

Spaans, M., & van Dishoeck, E. F. 2001, ApJ, 548, L217

Spinoglio, L., Giannini, T., Nisini, B., et al. 2000, A&A, 353, 1055

Swinyard, B. M., Clegg, P. E., Ade, P. A. R., et al. 1996, A&A, 315, L43

Tielens, A. G. G. M. 1989, in Interstellar Dust, ed. L. J. Allamandola, & A. G. G. M. Tielens, IAU Symp., 135, 239 (Dordrecht: Kluwer)

van der Tak, F. F. S., van Dishoeck, E. F., Evans, N. J., II, Bakker, E. J., & Blake, G. A. 1999, ApJ, 522, 991

van der Tak, F. F. S., van Dishoeck, E. F., & Caselli, P. 2000a, A&A, 361, 327

van der Tak, F. F. S., van Dishoeck, E. F., Evans, N. J., II, & Blake, G. A. 2000b, ApJ, 537, 283

van der Tak, F. F. S., Boonman, A. M. S., Braakman, R., & van Dishoeck, E. F. 2003, A&A, submitted

van Dishoeck, E. F., & Helmich, F. P. 1996, A&A, 315, L177

van Dishoeck, E. F. 1998, in Chemistry and Physics of Molecules and Grains in Space, Faraday Discussions, 109, 31

van Dishoeck, E. F., Wright, C. M., Cernicharo, J., et al. 1998, ApJ, 502, L173

van Zadelhoff, G. J., Dullemond, C. P., van der Tak, F. F. S., et al. 2002, A&A, 395, 373

Wilson, C. D., Mason, A., Gregersen, E., et al. 2003, A&A, 402, L59

Wright, C. M., van Dishoek, E. F., Helmich, F. P., et al. 1997, in the first ISO workshop on Analytical Spectroscopy, ESA SP, 419, 37

Wright, C. M., van Dishoeck, E. F., Black, J. H., et al. 2000, A&A, 358, 689